Stereodynamics in NO(X) + Ar inelastic collisions

M. Brouard,[1, a)] H. Chadwick,[1, b)] S. D. S. Gordon,[1] B. Hornung,[1, c)] B. Nichols,[1] F.J. Aoiz,[2, d)] and S. Stolte[3, e)]

[1)] *The Department of Chemistry, University of Oxford, The Chemistry Research Laboratory, 12 Mansfield Road, Oxford, OX1 3TA, United Kingdom.*[f)]

[2)] *Departamento de Química Física, Facultad de Química, Universidad Complutense, 28040 Madrid, Spain*

[3)] *Institute of Atomic and Molecular Physics, Jilin University, Changchun 130012, China.*[g)]

(Dated: 8 May 2016)

The effect of orientation of the NO(X) bond axis prior to rotationally inelastic collisions with Ar has been investigated experimentally and theoretically. A modification to conventional velocity-map imaging ion optics is described, which allows the orientation of hexapole state-selected NO(X) using a static electric field, followed by velocity map imaging of the resonantly ionized scattered products. Bond orientation resolved differential cross sections are measured experimentally for a series of spin-orbit conserving transitions and compared with quantum mechanical calculations. The agreement between experimental results and those from quantum mechanical calculations is generally good. Parity pairs, which have previously been observed in collisions of unpolarized NO with various rare gases, are not observed due to the coherent superposition of the two $j = 1/2$, $\Omega = 1/2$ Λ-doublet levels in the orienting field. The normalized difference differential cross sections are found to depend predominantly on the final rotational state, and are not very sensitive to the final Λ-doublet level. The differential steric effect has also been investigated theoretically, by means of quantum mechanical and classical calculations. Classically, the differential steric effect can be understood by considering the steric requirement for different types of trajectory that contribute to different regions of the differential cross section. However, classical effects cannot account quantitatively for the differential steric asymmetry observed in NO(X) + Ar collisions, which reflects quantum interference from scattering at either end of the molecule. This quantum interference effect is dominated by the repulsive region of the potential.

[a)]Electronic mail: mark.brouard@chem.ox.ac.uk

[b)]Current address: Laboratoire de Chimie Physique Moléculaire, Ecole Polytechnique Fédérale de Lausanne, Lausanne, Switzerland

[c)]School of Chemistry, University of Bristol, Cantock's Close, Bristol, BS8 1TS, United Kingdom

[d)]Electronic mail: aoiz@quim.ucm.es

[e)]Electronic mail: s.stolte@vu.nl

[f)]The Department of Chemistry, University of California, Berkeley, CA 94720, USA

[g)]Department of Physics and Astronomy, LaserLaB, Vrije Universiteit, Amsterdam, de Boelelaan 1081, 1081 HV Amsterdam, The Netherlands, and Laboratoire Francis Perrin, Batiment 522, DRECEM/SPAM/CEA Saclay, 91191 Gif sur Yvette, France

I. INTRODUCTION

The study of stereodynamics, in which the effect of a particular collision geometry on the outcome of a collision is assessed, plays an important role in many areas of chemistry. Knowledge of the steric requirements for a collision can help elucidate the mechanism by which chemical change takes place. In the past half decade, continuing advances in experiments and theory have allowed insight into a range of reactive and inelastic collisional processes.[1]

Many experiments have been performed in which the integral steric effect is probed. This quantity provides information on how the reaction or collision probability (or cross section) varies with the polarization of the either the reactant bond axis, $\boldsymbol{r}$, and/or rotational angular momentum, $\boldsymbol{j}$, with respect to the relative velocity, $\boldsymbol{k}$. Such measurements yield a wealth of information about the underlying mechanisms as well as quantum interference effects. Further insight is gained from the differential steric effect, in which the reactivity or scattering cross section is measured as a function of both the reactant polarization and direction of the final relative velocity, $\boldsymbol{k}'$.

For many years, investigation into the effect of bond orientation on the differential cross sections for reactive collisions has been used to elucidate the mechanisms underlying simple chemical reactions. The first such investigations employed hexapole focusing and subsequent manipulation with an electric field to orient symmetric top molecules such as CH_3I prior to collisions with metal atoms such as K or Rb.[2–7] Development of the brute force orientation technique[8] allowed extension of this work to orient larger molecules, such as iodobenzene and iodotoluene during collisions with K.[9,10] In these investigations, the observed differential steric preference was found to be well explained by a cone of acceptance/exclusion model.[9] This assumes a mechanism with a linear R–I–K transition state in which an electron jumps from the K atom to the molecule at some distance, R, resulting in an anionic state of the molecule which rapidly dissociates. As the molecule dissociates, the K^+ and I^- ions rebound in the backwards scattered direction, interacting with the R fragment, resulting in a cone of ejection in which the products are found. Investigation of the Li + HF ($v = 1$) reaction using optical methods to prepare an aligned distribution of the rotational angular momentum of the HF, and therefore of the bond axis, showed a propensity for end on collisions to result in backwards scattered products.[11,12]

A series of recent experiments[13–15] investigated the effect of alignment of the C-H bond of $CD_3H(v = 1)$ before a collision with Cl. By performing the experiment in eight different geometries, Wang *et al.* were able to extract the j-PDDCSs that fully characterise the preference of the reaction on the alignment of the C-H bond. It was found that HCl ($v = 0$) is formed as a product of direct collisions, which can be well-described by a classical line of centres model.[14]

The technique of hexapole state selection, followed by orientation with a static electric field, has also been employed to investigate the integral steric effect in collisions of both NO(X)[16–20] and OH(X).[21–25] Specifically these experiments measured the integral steric asymmetry, defined for NO as

$$S = \frac{\sigma_{\mathrm{N}} - \sigma_{\mathrm{O}}}{\sigma_{\mathrm{N}} + \sigma_{\mathrm{O}}}, \tag{1}$$

i.e. the normalized difference of the integral cross sections for scattering from the 'N' and 'O' ends of the molecule. For collisions of NO(X) with He and Ar, the steric asymmetry was found to be large in magnitude, and alternated in sign between positive and negative values with final rotational state, j'.[16–20,26] This alternation effect was attributed to quantum interference from scattering from either end of the molecule, which was confirmed using a quasi-quantum treatment (QQT).[19] A recent extension of this work to determine bond orientation resolved differential cross sections for the NO(X) + Ar system demonstrated that this quantum interference was also evident in the differential steric effect.[27] Quantum interference was found to increase from low to intermediate Δj, where it was most pronounced, whilst at high Δj, the integral and differential steric effects could be well-accounted for by classical mechanics.[19,27] In contrast to collisions of NO(X), studies of the steric asymmetry in OH(X) + He and Ar systems found that the integral steric asymmetry did not show strong quantum interference effects and could be explained using a classical ball and stick model.[22] The difference in behaviour arises because NO(X) is a near-homonuclear molecule, whilst OH(X) is highly heteronuclear and asymmetric with respect to the center-of-mass. Differences in behaviour may also arise from the fact that NO(X) conforms most closely to a Hund's case (a) molecule, whilst OH(X) is closer to Hund's case (b) for the range of rotational states typically accessed.

Velocity map[28] ion imaging[29] has proved to be a powerful technique for determining scattering angle distributions (related to the $\boldsymbol{k} - \boldsymbol{k}'$ correlation) in both reactive and inelastic collisions. By adapting conventional velocity mapping ion optics, it is possible to introduce

a static electric field into the scattering centre,[30] allowing the orientation of species such as NO(X) by exploiting the Stark effect.[27] In Section III we provide details of such modifications. Experimentally determined bond orientation resolved differential cross sections for spin-orbit conserving collisions of NO(X) + Ar will be presented in IV A and compared with quantum mechanical calculations. In sections IV B and IV C, the differential steric effect in collisions of NO(X) + Ar will be investigated in the classical and quantum mechanical frameworks, respectively.

II. ORIENTED MOLECULE SCATTERING

NO(X) is a $^2\Pi$ molecule, with one unpaired electron in a π^* orbital. The unpaired electron gives rise to two spin-orbit manifolds, $^2\Pi_{\frac{1}{2}}$ and $^2\Pi_{\frac{3}{2}}$, which are separated by approximately $123\,\mathrm{cm}^{-1}$. Within each spin-orbit manifold, the rotational wavefunctions are given by a symmetric ($\epsilon = +1, e$) and antisymmetric ($\epsilon = -1, f$) combination of the $+\Omega$ and $-\Omega$ states

$$|jm\Omega\epsilon\rangle = \frac{1}{\sqrt{2}}\left[|jm+\Omega\rangle + \epsilon|jm-\Omega\rangle\right] . \tag{2}$$

At low j, the two $\epsilon = \pm 1$ levels, known as the Λ-doublet, are nearly degenerate, however they differ in their parity $p = (-1)^{j-\epsilon/2}$. The interaction of the NO(X) with a rare gas atom during a collision leads to two potential energy surfaces of A' and A'' symmetry, labelled with respect to the reflection symmetry in the triatomic plane. For Hund's case (a) molecules, it has been shown that spin-orbit conserving and changing transitions can be considered to take place on the V_{sum} and V_{diff} potentials respectively, which are half sum and half difference combinations of the A' and A'' potentials.[31,32]

The initial quantum state of the NO(X) molecule is selected using a hexapole electric field, which exploits the Stark effect to focus only the $|\Omega = 0.5, j = 0.5, \epsilon = -1, f\rangle$ state into the interaction region. The first-order Stark interaction energy is given by

$$W_{\mathrm{Stark}} = -\langle \boldsymbol{\mu}.\boldsymbol{E}\rangle = -\mu E \langle \cos\Theta_{\mu E}\rangle_{\max} = -\epsilon\mu E \frac{|\Omega m|}{j(j+1)} , \tag{3}$$

where $\boldsymbol{\mu}$ is the static dipole moment of NO(X) and $\boldsymbol{E}$ is the applied static electric field, with $\Theta_{\mu E}$ the angle between the two. The $\epsilon = -1, f$ component of the Λ-doublet thus experiences an increase in energy in the presence of an electric field and as such is low field seeking and will be focused by the hexapole field. In contrast, the $\epsilon = +1, e$ component will be high field

This manuscript was accepted by J. Chem. Phys. Click here to see the version of record.

inking and experiences a force that deflects these molecules from the path of the molecular beam.

In order to orient the molecular bond axis, the state selected molecules are exposed to a static electric field in the scattering centre. In an applied static electric field, the wavefunction of the NO(X) can be written as a combination of the field free f and e states

$$|jm\Omega E\rangle = \frac{1}{\sqrt{2}}\left[\alpha|jm\Omega e\rangle + \beta|jm\Omega f\rangle\right] . \tag{4}$$

When the direction of the electric field is along the initial relative velocity, the absolute values of α and β are given by

$$|\alpha| = +\sqrt{1 - \frac{1}{\sqrt{1+E_{\rm red}^2}}} \qquad |\beta| = +\sqrt{1 + \frac{1}{\sqrt{1+E_{\rm red}^2}}} , \tag{5}$$

where

$$E_{\rm red} = \frac{2W_{\rm Stark}}{W_\Lambda} , \tag{6}$$

and W_Λ is the Λ-doublet splitting between the e and f states. Note that this expression does not change if $|jm\Omega E\rangle$ is multiplied by an arbitrary phase factor. Hence, the relative signs of α and β determine whether the NO bond axis, $\boldsymbol{r}$, which points from the N-atom to the O-atom, tends to be oriented parallel or antiparallel to the relative velocity of the NO molecule with respect to the Ar atom.[27] In the high field limit, an N-end favoring collision geometry, with $\boldsymbol{r}$ parallel to $\boldsymbol{k}$, corresponds to $\alpha = \beta = 1$ and an O-end favoring collision geometry with $\boldsymbol{r}$ antiparallel to $\boldsymbol{k}$ corresponds to $\alpha = -1, \beta = 1$, whilst if there is no applied field, $\alpha = 0$ and $\beta = \sqrt{2}$, such that the non-oriented f state wavefunction is recovered from Eq. (4). This sign convention is chosen to ensure that the 'N'-end of NO points towards the negative electrodes of the four rod assemble, as described further in the following section. Note also that Eqs. (5) and (6) ignore the effects of the hyperfine interaction, which has been shown to be a reasonable approximation in the case of NO(X) at the field strengths employed.[33]

Using the symmetrized wavefunctions for the e and f levels, the oriented states given in Eq. (4) can be rewritten as

$$|jm\Omega E\rangle = \frac{1}{2}\left[(\alpha+\beta)|jm\Omega\rangle + (\alpha-\beta)|jm-\Omega\rangle\right] . \tag{7}$$

Expressing the $|jm\Omega\rangle$ ket in the coordinate representation, the wavefunction can be written as

$$|jm\Omega\rangle = \sqrt{\frac{2j+1}{8\pi^2}}\, D^j_{m\Omega}(\Phi_{\mu E}, \Theta_{\mu E}, \chi_{\mu E})^* \tag{8}$$

This manuscript was accepted by J. Chem. Phys. Click here to see the version of record.

where $(\Phi_{\mu E}, \Theta_{\mu E}, \chi_{\mu E})$ are the Euler angles that define the direction of the static dipole moment with respect to the laboratory frame in which the orienting electric field defines the Z-axis. The extrinsic probability distribution for the orientation of the bond axis (which lies parallel to the dipole) can be written as[26,34]

$$P(\Theta_{\mu E}) = \frac{2j+1}{32\pi^2}\int_0^{2\pi}\int_0^{2\pi} \Big|(\alpha+\beta)D^j_{m\Omega}(\Phi_{\mu E},\Theta_{\mu E},\chi_{\mu E}) + (\alpha-\beta)D^j_{m-\Omega}(\Phi_{\mu E},\Theta_{\mu E},\chi_{\mu E})\Big|^2 \mathrm{d}\Phi_{\mu E}\,\mathrm{d}\chi_{\mu E}\,, \tag{9}$$

which results in

$$P(\Theta_{\mu E}) = \frac{2j+1}{8}\{\left[(\alpha+\beta)d^j_{m\Omega}(\Theta_{\mu E})\right]^2 + \left[(\alpha-\beta)d^j_{m-\Omega}(\Theta_{\mu E})\right]^2\}\,, \tag{10}$$

where $d^j_{m\Omega}(\Theta_{\mu E})$ are the reduced Wigner rotation matrix elements. For the $j = 1/2$, $m = \pm 1/2$, $\Omega = \pm 1/2$, we can therefore write[21,34]

$$P(\Theta_{\mu E}) = \frac{1}{4}\left[(\alpha+\beta)^2\cos^2(\Theta_{\mu E}/2) + (\alpha-\beta)^2\sin^2(\Theta_{\mu E}/2)\right]\,, \tag{11}$$

or

$$P(\Theta_{\mu E}) = \frac{1}{4}[\alpha^2+\beta^2+2\alpha\beta\cos(\Theta_{\mu E})] = \frac{1}{2}[1+\alpha\beta\cos\Theta_{\mu E}]\,. \tag{12}$$

Under these conditions, and in the limit of high fields when $\alpha = \beta = 1$, the average value is $\langle\cos\Theta_{\mu E}\rangle_{\max} = \frac{1}{3}$.

III. EXPERIMENTAL DESIGN AND SIMULATIONS

The experimental apparatus used in this study has been described in detail elsewhere,[27,35–37] and so only the details relevant to the current work will be given here. The experiments employ a crossed molecular beam apparatus, combined with $(1+1')$ resonance enhanced multi-photon ionisation (REMPI) and velocity-map ion imaging. The primary and secondary molecular beams are generated using General valves containing 15% NO seeded in Ar and neat Ar respectively. Pulsing the primary and secondary valves at 10 Hz and 5 Hz, respectively, allows on-the-fly subtraction of unscattered NO from the experimental images. The NO molecular beam is doubly skimmed and then state selection is achieved using a hexapole field as described in the previous section. The $|\Omega = 0.5, j = 0.5, f\rangle$ state is focused into the scattering region, where it is exposed to a static electric field to allow orientation of

ing NO bond axis either parallel or antiparallel to the relative velocity. After the scattering has taken place, the rotationally excited NO(X) is state selectively excited to NO(A), using the 226 nm output of a Lambda Physik dye laser. The NO(A) molecules are then ionised using 308 nm radiation from an XeCl excimer laser. Following ionization, the NO^+ ions are velocity mapped onto a position sensitive detector consisting of multi-channel plates and a P43 phosphor screen.

In order to measure the bond orientation resolved differential cross sections, it was necessary to modify the experimental apparatus[36–38] such that the NO molecular bond axis can be oriented using a static electric field prior to the collision. In this section the development of the experimental modifications will be discussed and the final experimental design and method presented.

Fig. 1 shows calculated quantum mechanical DCSs for a range of electric field strengths for 'N' end (left panel) and 'O' end (right panel) collisions. The calculations were performed including only the first order, linear Stark effect, but very similar results are obtained with inclusion of the second order Stark effect. From these calculations it can be seen that increasing the applied field from 10 kV/cm to an infinite field does not have a large effect on the calculated DCS. Therefore an electric field on the order of 10 kV/cm should be sufficient to observe differences in the 'N' end and 'O' end DCSs.

The static electric field needed to orient the NO(X) molecule can be generated by introducing four orientation electrodes in between the repeller and extractor plates, as shown in panel a) of Fig. 2. However, before the scattered NO is ionised using $(1 + 1')$ REMPI, the electric field needs to be rapidly switched such that the NO^+ ions can be velocity mapped onto the detector. The presence of the orientation electrodes near the detection region will result in distortions to the velocity mapping electric field. The feasibility of introducing orientation electrodes near the detection region was investigated using SIMION 8.0 to perform ion trajectory simulations.[39]

The ion optics consist of three electrodes: a repeller, extractor and a ground electrode and the orientation electrodes consist of four rod shaped electrodes. Voltages were applied to all electrodes except the ground electrode. Panel a) of Fig. 2 details the dimensions of the ion optics, with d indicating the horizontal spacing between the orientation electrodes. As in the experimental apparatus, a field free time of flight tube extends a further 62.5 cm beyond the ground electrode.

The detection volume in the experiment is determined by the overlap of the beam profiles of the excitation and ionisation lasers. The ions used in the simulation were created in the detection volume, halfway between the repeller and extractor and in the center of the orientation electrodes. The detection volume was simulated as a 3D Gaussian distribution with standard deviations of 0.2 mm in each of the x, y and z directions. These initial conditions result in ions created in a cube approximately 1 mm × 1 mm × 1 mm. This is slightly smaller than the detection volume used in previous experiments,[35] which has been achieved using an iris to reduce the size of both laser beams.

The quality of the velocity mapping was determined by plotting the x or y components of the initial velocity against the final x or y position on the detector. Such a plot should be linear for good velocity mapping. Panel b) of Fig. 2 shows plots of initial velocity against final position on the detector resolved into x and y components for different horizontal spacings of the orientation electrodes. In the simulations, the y-axis is parallel to the orientation electrodes and the x-axis is perpendicular. In all cases, the linear fit to the plots has a correlation coefficient, R^2, value of greater that $R^2 = 0.999$. However, as the horizontal spacing of the orientation electrodes increases, any distortions to the velocity mapping field decrease, and so the R^2 value becomes closer to 1. It is also noticeable that at a spacing of $d = 10$ mm, the gradients of the x-component and y-component lines are slightly different, reflecting different magnifications in either direction. As a consequence of this, the ion image will be stretched in the direction parallel to the orientation rods (y direction) and thus will no-longer be circular. As the spacing between the orientation electrodes is increased, the effect of this distortion decreases such that at a 30 mm spacing the gradients of the two lines are identical and the observed ion image would be circular.

Another effect of changing the spacing between the rod electrodes is on the strength of the orientation field achievable. At the largest spacing included in the simulations, $d = 30$ mm, the field in the scattering region is 2.0 kV/cm with a voltage of ±8 kV applied to the rod electrodes. In contrast, a field of 9.2 kV/cm can be obtained with a reduced spacing of $d = 10$ mm. There is, therefore, a trade-off between the degree of orientation in the experiment and the quality of the velocity mapping. In Fig. 3, calculated DCSs for electric fields corresponding to rod spacings of 30 mm, 20 mm and 10 mm are displayed, along with simulated ion images. The vertical distance between the rods is fixed at 10 mm. For a rod spacing of 30 mm, the simulated image is almost circular, however, very little difference is

This manuscript was accepted by J. Chem. Phys. Click here to see the version of record.

observed between the two calculated DCSs (and therefore the corresponding ion images) due to the low electric field strength. On the other hand, with a rod spacing of 10 mm, significant differences between the 'N' and 'O' end DCSs can be observed. The distorting effect of the orientation electrodes on the image has been incorporated into the simulation and fitting procedures, which have been described in detail previously,[35,36,38] to account for the non-circular appearance of the ion image. Therefore a rod electrode spacing of 10 mm was selected in order to maximise the orientation field achievable. At this electric field, the mixing coefficients α and β, defined by Eq. (5), take values of 0.64 and 1.26, respectively.

It should be noted that even with an increased spacing between the orientation electrodes, it is possible to augment the orientation field by applying a voltage to the repeller and extractor electrodes as described by Lipciuc *et al.*[30] By splitting the repeller and extractor in half, ± 8 kV could be applied to each half of the ion optic electrode, augmenting the orientation field in the detection volume. Simulations suggest that with an orientation electrode spacing of 26 mm, an orientation field of 9 kV/cm would be achievable. This could provide a method of improving the velocity mapping should it be required for future experiments.

Details of the relative directions of the molecular beams, laser beams and orientation electrodes can be found in Refs. 27 and 1. The ± 8 kV is applied to the two pairs of orientation electrodes, such that an electric field of 9.2 kV/cm is directed either parallel or antiparallel to the direction of the relative velocity. To ensure velocity mapping conditions when the NO is ionised, Belkhe switches are employed to rapidly switch the voltages applied to the orientation rods approximately 100 ns before the lasers fire.[27] After the switching, 900 V is applied to each of the rods. The extraction field employed to velocity map the NO^+ ions is not sufficient to mix the Λ-doublet levels of the scattered NO and orient the molecule, with $\alpha < 0.01$ in the extraction field. The voltages on the repeller and extractor are held constant throughout at voltages of 1500 V and 650 V, respectively. The delay between the switching of the voltages and the laser firing was set to be as short as possible, whilst still retaining good velocity mapping. Investigation of the magnitude of the integral steric asymmetry as a function of delay between switching and firing time indicated that delays of up to 1 μs had very little effect on the observed steric asymmetry. This is perhaps not surprising as the molecular beams have time profiles of many hundreds of microseconds, so the fraction of collisions that occur in 100 ns will be very small. A minimum delay of 100 ns was used

ing record the data presented here in order to ensure that the switching was fully complete when the laser fires. After 1000 laser shots, the direction of the orienting field is reversed to allow alternate recording of 'N' and 'O' end images. The polarization of the excitation radiation is alternated between horizontally and vertically polarized light on a shot-by-shot basis.

Based on the simulations of the experiment, we estimate that the angular resolution under typical operating conditions is around 15° on average, although it displays some dependence on scattering angle. This resolution is sufficient to resolve most of the interesting features in the differential steric effect, apart from the rapid diffraction oscillations observed in the forward scattered direction at low Δj.[40]

IV. RESULTS AND DISCUSSION

A. Bond orientation resolved differential cross sections

Experimental images for spin-orbit conserving collisions of oriented NO(X) with Ar are shown in Figs. 4 and 5, along with simulations performed using the QM calculated bond orientation resolved DCS. For transitions to final e states, the $Q_{21}+R_{11}$ overlapping branches were used, whilst the R_{21} branch was employed to detect the scattered NO into f states. As can be seen, the agreement between experimental and simulated images is generally very good. The 'N' and 'O' end images are color scaled to preserve their relative intensities, with the maximum intensity of either the 'N' and 'O' end image colored red. The images are slightly distorted from circularity in the direction perpendicular to the relative velocity (and therefore parallel to the rods), due to the effect of the orientation electrodes on the velocity mapping field as predicted in Section III. This effect has been incorporated into the simulation and fitting procedures[35,36] and so the same distortion is evident in the QM simulations. The images also show a distinct asymmetry with respect to reflection in the relative velocity, which is a consequence of the different detection efficiencies for molecules with different laboratory frame velocities.

A number of general trends can be seen in the bond orientation resolved ion images, similar to those observed for collisions of unpolarized NO(X) with Ar[35] and He.[41] The extent of the intensity in the experimental and simulated images decreases as the rotational exci-

region increases and a greater proportion of the collision energy is transferred to rotational motion, resulting in a smaller outgoing velocity of the NO. As for scattering without an orienting field, the peak in intensity in the ion images also shifts from forwards scattered at low rotational excitation to sideways and increasingly backwards scattered as the rotational excitation increases. This can be attributed to the propensity for low rotational excitation to result from large impact parameter, glancing blow collisions that result in forwards scattered molecules, whereas high rotational excitation requires impulsive, small impact parameter collisions leading to backwards scattered NO. For all the transitions recorded, differences between the images for 'N' end and 'O' end collisions are apparent, in both the experimental and simulated images.

Figs. 6 and 7 show a comparison of the experimentally determined bond orientation resolved DCSs with corresponding quantum mechanical calculations for spin-orbit conserving transitions to final e and f states, respectively. The experimental data has been scaled to the QM DCS, with the same scaling factor applied to both the 'N' and 'O' end DCSs. The agreement between the experimentally determined bond orientation resolved DCSs and QM calculations is, in general, good. The experimental fits capture some of the subtle differences in structure between 'N' and 'O' end DCSs, such as the second peak at 120° in the 'N' end DCS for $j' = 11.5, f$, which is not seen for the corresponding 'O' end collision. The most significant disagreement is found for $j' = 9.5, e$, for which the intensity in the experimental image in concentrated in the slow lab frame velocity region of the image. This state is therefore very sensitive to the parameters used to generate the flux density correction, and will be more susceptible to errors in its determination. In general, the orientation of the bond axis prior to the collision can be seen to have a significant effect on the relative intensities of the observed and theoretically predicted peaks in the DCS, however the position and number of observed peaks is not changed. In previous studies of the integral steric asymmetry,[16–19,26,27] large oscillations were observed for middle rotational excitation, with odd and even j' transitions showing 'N' and 'O' end preferences respectively. This effect can also be observed in the current data, with 'N' end images for odd j' transitions being more intense than the corresponding 'O' end images (and vice versa).

In previous work on collisions of NO(X) + He, Ne, Ar and Kr,[35–38,41–44] parity pairs were observed, for which the DCSs for a $j' = n + 0.5, f$ state is very similar to the DCS for the corresponding $j' = n - 0.5, e$ state. An example of such a parity pair, for which $n = 10$, is

$j' = 9.5, e$ and $j' = 10.5, f$. Whilst similar structures can be seen in the DCSs for each state, the similarity is not as striking as for collisions in which the initial bond axis orientation is not selected.[35] When the $|\Omega = 0.5, j = 0.5, f\rangle$ state that is selected by the hexapole is exposed to a static electric field in the interaction region, a coherent superposition of the field free $|f\rangle$ and $|e\rangle$ Λ-doublet levels is created, such that the wavefunction of the NO(X) is given by Eq. (4). Although the final state after the collision can be considered field free, possessing a definitive parity, the initial state state is not, and it is therefore no longer correct to consider individual transitions as 'parity conserving' or 'parity changing', as the NO(X) molecule has mixed f and e character before the collision.

B. Classical steric effect

Classically, the differential cross section for a collision of oriented NO(X) with Ar can be written in terms of 'intrinsic' and 'extrinsic' polarization moments.[12,45,46] Extrinsic polarization moments describe the reagent polarization as a result of the preparation of the system, in the laboratory. These moments are a consequence of external circumstances, and do not depend on the steric preferences of the collision. In contrast, the intrinsic polarization moments describe the steric preference of the collision. These intrinsic moments are dependent only on the dynamics of the collision and are not affected by the preparation of the system. The quasi-classical treatment of the $\boldsymbol{k} - \boldsymbol{r} - \boldsymbol{k'}$ vector correlation has been presented in detail in Ref. 12 and only the most significant equations will be considered here.

The *intrinsic* inelastic collision probability density function into a given scattering angle, θ, for an internuclear axis direction given by θ_r and ϕ_r can be written as an expansion in modified spherical harmonics, $C^*_{kq}(\theta_r, \phi_r)$, as

$$P(\theta, \theta_r, \phi_r) = \frac{1}{4\pi} \sum_k \sum_{q=-k}^{+k} [k] R^{(k)}_q(\theta) C^*_{kq}(\theta_r, \phi_r)\,, \tag{13}$$

where the scattering angle dependent $R^{(k)}_q(\theta)$ are the *r-polarization dependent differential cross sections*, r-PDDCSs, which quantify the dependence of the collision on the polarization of the bond axis as a function of scattering angle. Their meaning is analogous to the j-PDDCSs[45–47] except for the fact that they contain information about how the direction of the bond axis, $\boldsymbol{r}$, influences the reactivity, while the j-PDDCSs are concerned with the role of the direction of the reactant rotational angular momentum, $\boldsymbol{j}$. The direction of $\boldsymbol{r}$ is

This manuscript was accepted by J. Chem. Phys. Click here to see the version of record.

specified by the polar and azimuthal angles θ_r and ϕ_r with respect to the scattering frame, whose z axis is along the initial relative velocity, $\boldsymbol{k}$, and whose $x-z$ plane contains both the initial, $\boldsymbol{k}$, and final, $\boldsymbol{k}'$, relative velocities. The symbol $[k] \equiv 2k+1$.

The r-PDDCS are the multipole moments of the expansion, and in QCT calculations are given by

$$R_q^{(k)}(\theta) = \int P(\theta, \theta_r, \phi_r) C_{kq}(\theta_r, \phi_r) \mathrm{d}\,\omega_r = \langle C_{kq}(\theta_r, \phi_r) \rangle \,, \tag{14}$$

where $\mathrm{d}\omega_r = \mathrm{d}(\cos\theta_r)\mathrm{d}\phi_r$. The distribution of reagent internuclear axes is invariant with respect to reflection in the $\boldsymbol{kk'}$ plane. Consequently $P(\theta, \theta_r, \phi_r) = P(\theta, \theta_r, 2\pi - \phi_r)$. It can be easily shown that the r-PDDCSs are real quantities:

$$R_q^{(k)}(\theta) = (-1)^q R_{-q}^{(k)}(\theta) = [R_q^{(k)}(\theta)]^* \,. \tag{15}$$

As in the case of the j-PDDCSs, the monopole $R_0^{(0)}(\theta)$ term is nothing but the normalized DCS or angular distribution in the absence of NO orientation, that is, $(2\pi/\sigma)\ \mathrm{d}\sigma/\mathrm{d}\omega$.

The oriented (and/or aligned) differential cross section is given by convoluting the intrinsic distribution with the extrinsic one, which corresponds to the preparation of the internuclear axis prior to the collision:[45,47]

$$\left[\frac{\mathrm{d}\sigma}{\mathrm{d}\omega}\right]_{\text{orient}} = \frac{\sigma_{\text{iso}}}{2\pi} \sum_k \sum_{q=-k}^{k} [k] R_q^{(k)}(\theta) a_q^{(k)} \,, \tag{16}$$

where σ_{iso} is the integral cross section for the collision without axis orientation of the NO and $a_q^{(k)}$ are the moments that describe the bond axis extrinsic polarization with respect to the $\boldsymbol{k}$-$\boldsymbol{k}'$ scattering frame. Since the bond axis distribution is prepared in the laboratory frame, whose Z axis lies along the electric field, a transformation is needed to determine values of the scattering frame moments, which in the case of cylindrically symmetric distributions may be written[45,46]

$$a_q^{(k)} = \sum_{q'=-k}^{k} D_{qq'}^{k*}(\phi_E, \theta_E, \chi_E) A_{q'}^{(k)} = C_{kq}(\theta_E, \phi_E) A_0^{(k)} \,, \tag{17}$$

where $D_{qq'}^k(\phi_E, \theta_E, \chi_E)$ is a Wigner rotation matrix and $(\phi_E, \theta_E, \chi_E)$ are the Euler angles that relate the laboratory frame with the scattering frame. The $A_q^{(k)}$ polarization moments describe the polarization of the reactant in the laboratory frame (see further below). Given the axial symmetry of the bond axis (or dipole moment) about the electric field in the laboratory frame, the only non-zero polarization moments in the laboratory frame are those

This manuscript was accepted by J. Chem. Phys. Click here to see the version of record.

with q=0. Consequently, χ_E can be taken as zero, and the the rotation matrix is equal to the corresponding modified spherical harmonic, $C_{kq}(\theta_E, \phi_E)$.

Taking into account the symmetry properties of the $R_q^{(k)}(\theta)$ given by Eq. (15), the differential cross section when the direction of the electric field is defined by θ_E and ϕ_E can be written as[12]

$$\left[\frac{\mathrm{d}\sigma}{\mathrm{d}\omega}\right]_{\theta_E}^{\phi_E} = \frac{\sigma_{\mathrm{iso}}}{2\pi} \sum_k [k] A_0^{(k)} \sum_{q=0}^{k} \frac{2}{1+\delta_{q0}} R_q^{(k)}(\theta)\, C_{kq}(\theta_E, 0) \cos q\phi_E \,. \tag{18}$$

In the present case, the electric field is directed parallel or antiparallel to $\boldsymbol{k}$, so $\theta_E = 0°$ for 'N' end collisions and $\theta_E = 180°$ for 'O' end collisions, whereas ϕ_E is undetermined (it can take any value and hence can be made equal to zero) in both cases.

As shown in Section II, the laboratory frame bond axis extrinsic distribution given in Eq. (12) can be written, integrated over the azimuthal angle, ϕ, as

$$P(\theta_{\mu E}) = \frac{1}{4}(\alpha^2+\beta^2)\left[1 + \frac{2\alpha\beta}{\alpha^2+\beta^2} P_1(\cos\theta_{\mu E})\right] , \tag{19}$$

where $P_1(\cos\theta_{\mu E})$ is the 1st degree Legendre polynomial given by $P_1(\cos\theta_{\mu E}) = \cos\theta_{\mu E}$. The lab frame orientation moment, $A_0^{(1)}$, is given by the expectation value $A_0^{(1)} = \langle P_1(\cos\theta_{\mu E})\rangle$,[48] which can be calculated as

$$\begin{aligned} \langle P_1(\cos\theta_{\mu E})\rangle &= \int_{-1}^{1} P_1(\cos\theta_{\mu E}) P(\theta_{\mu E}) \mathrm{d}(\cos\theta_{\mu E}) \\ &= \frac{1}{3}\frac{2\alpha\beta}{\alpha^2+\beta^2} = \frac{1}{3}\alpha\beta \,. \end{aligned} \tag{20}$$

In the high field limit, the orientation moment $A_0^{(1)} = \langle P_1(\cos\theta_{\mu E})\rangle$ is therefore equal to 1/3. The $A_0^{(0)}$ moment is equal to unity as the distribution is normalized. Eq. (16) can be written in terms of the laboratory frame moments as[12]

$$\left[\frac{\mathrm{d}\sigma}{\mathrm{d}\omega}\right]_{\theta_E}^{\phi_E} = \frac{\sigma_{\mathrm{iso}}}{2\pi}\left\{R_0^{(0)}(\theta) + 3A_0^{(1)}\left[R_0^{(1)}(\theta) P_1(\cos\theta_E) + 2R_1^{(1)}(\theta) C_{11}(\theta_E, 0)\cos\phi_E\right]\right\} , \tag{21}$$

however, as $\phi_E = 0°$ and $\theta_E = 0°$ or 180°, $C_{11}(\theta_E, \phi_E) = 0$, so only the first two terms of Eq. (21) contribute to the oriented DCS. The observed DCS is thus given by

$$\left[\frac{\mathrm{d}\sigma}{\mathrm{d}\omega}\right]_{\theta_E} = \frac{\sigma_{\mathrm{iso}}}{2\pi}\left[R_0^{(0)}(\theta) + \alpha\beta R_0^{(1)}(\theta) P_1(\cos\theta_E)\right] . \tag{22}$$

Therefore, to a good approximation, only the normalized DCS without orientation, $R_0^{(0)}(\theta)$, and the k=1, q=0, r-PDDCS, $R_0^{(1)}(\theta)$, contribute to the observed DCS. Eq. (22) can be also

written as

$$\left[\frac{\mathrm{d}\sigma}{\mathrm{d}\omega}\right]_{\theta_E} = \left[\frac{\mathrm{d}\sigma}{\mathrm{d}\omega}\right]_{\mathrm{iso}} \left[1 + \alpha\beta \frac{R_0^{(1)}(\theta)}{R_0^{(0)}(\theta)} P_1(\cos\theta_E)\right] , \tag{23}$$

$R_0^{(1)}(\theta)/R_0^{(0)}(\theta)$ is the *renormalized* r-PDDCS,[12,45,47] and $(\mathrm{d}\sigma/\mathrm{d}\omega)_{\mathrm{iso}}$ is the DCS without NO orientation. It should be mentioned that Eqs. (21)–(23) are also valid in the QM treatment, substituting the classical r-PDDCSs by their QM counterparts.

The details of the quasi-classical trajectory (QCT) calculations presented in this section have been described in detail elsewhere,[12] and so only those aspects relevant to this work will be given here. The calculations employed the V_{sum} potential energy surface of Alexander[49] and were run at a collision energy of 530 cm^{-1}, which corresponds to the experimental mean collision energy. The N-O internuclear distance was fixed at the equilibrium bond length, both in the calculation of the potential energy surface[49] and the subsequent QCT calculations. The maximum value of the impact parameter was set to 6.3 Å, beyond which no inelastic scattering was observed. The magnitude of the rotational angular momentum was allowed to vary continuously throughout the collision and was rounded to the nearest integer at the end of each trajectory to allow for comparison with quantum mechanical calculations. A total of 5×10^6 trajectories were run to allow determination of the bond orientation resolved DCSs and r-PDDCSs presented in this section.

Fig. 8 displays QCT bond orientation resolved DCSs for a range of Δj transitions, which have been calculated using Eq. (22) with the QCT $R_0^{(1)}(\theta)$ and $R_1^{(1)}(\theta)$ normalized r-PDDCSs, which are also shown in the figure. Clear differences between 'N' and 'O' end collisions can be seen for all states. For low rotational excitation ($\Delta j = 3$), the DCSs for the two orientations are very similar other than in the region of the secondary maxima at approximately $\theta = 25°$ for collisions with the 'N' end. This secondary maxima in the DCS for low Δj transitions can be attributed to ℓ-type rainbow scattering resulting from high impact parameter collisions which are deflected by the attractive part of the potential to the far side of the molecule.[50,51] In the region of the ℓ-type rainbow, the DCS for 'N' end scattering is larger than for corresponding 'O' end collisions. The normalized $R_0^{(1)}(\theta)$ moment can be seen to be positive in this region, indicating an 'N' end preference for these collisions and is approximately 0 elsewhere. Since the 'N' end of the molecule is displaced further from the centre of mass than the 'O' end, collisions with the 'N' end can exert more torque on the molecule and therefore a greater proportion of these large impact parameter collisions

result from 'N' end collisions. It can be seen that this effect is only important for these rainbow trajectories, as the 'N' and 'O' end DCSs are very similar over the remainder of the angular range and so only a small overall 'N' end preference was seen in the integral steric asymmetry presented in Ref. 27. For high rotational excitation, $\Delta j = 15$, an overall 'N' end preference is again observed, with the DCS for collisions with the 'N' end of the molecule taking larger values than 'O' end collisions and therefore the $R_0^{(1)}(\theta)$ normalized r-PDDCS is positive over almost the entire angular range. This can be explained using a classical ball and stick model; 'N' end collisions can exert more torque on the molecule and thus result in greater rotational excitation than 'O' end collisions.

In contrast, for $\Delta j = 7$ and 10, no strong overall preference for either 'N' or 'O' end collisions is seen, with the normalized $R_0^{(1)}(\theta)$ moment oscillating between positive and negative values indicating 'N' end preference at some angles and 'O' end preference at others. This effect can be rationalized by considering the QCT DCSs and deflection functions for an isotropic bond axis distribution of NO. Fig. 9 shows the QCT DCS for $\Delta j = 7$ and 10, for all trajectories, and resolved into collisions between $0° \leq \theta_r \leq 45°$ ('N' end) and $135° \leq \theta_r \leq 180°$ ('O' end), where θ_r is the angle between the NO bond axis, $\boldsymbol{r}$, and the relative velocity, $\boldsymbol{k}$. Note that this is not the same as the bond orientation resolved 'N' and 'O' end DCSs, as the laboratory frame bond axis distribution is not considered.

The total DCS appears as a single, broad peak for $\Delta j = 7$, with some evidence of multiple peaks for $\Delta j = 10$. However, by resolving the DCS into specific ranges of θ_r, a number of different contributions to the total DCS can be observed. Multiple peaks can be clearly seen in the 'O' end angular range resolved DCSs for both states. The origins of these multiple peaks can be elucidated by considering the deflection function and plots of positions of closest approach for these collisions, shown in the right panels of Fig. 9. There are two distinct regions of the deflection function that contribute to the 'O' end angular range resolved DCS. At high impact parameters, scattering through small angles is observed, whereas collisions at smaller impact parameters result in scattering through larger angles. This can be rationalised by considering the position of closest approach plots in the right hand column of Fig. 9. Some high impact parameter trajectories that start, for example, towards the 'O' end of the molecule ($135° \leq \theta_r \leq 180°$), are able to scatter from the 'N' end of the molecule as depicted in panel b) of Fig. 10 and vice versa. These will be referred to as 'far end' collisions. Since collisions with the 'N' end of the molecule can

exert more torque than collisions with the 'O' end, for collisions that result in a specific Δj transition, trajectories that collide towards the 'N' end of the molecule result from higher impact parameter, smaller scattering angle collisions. Therefore, the angular resolved DCS for 'O' end collisions consists of two contributions, one from 'near end', smaller impact parameter collisions in which the atom impinges towards the 'O' end of the molecules and the other from 'far end' high impact parameter collisions where the impact occurs towards the 'N' end of the molecule. These peaks are well separated in scattering angle, and therefore observed as two distinct peaks in the angular range resolved 'O' end DCS.

For $\Delta j = 7$, it can be seen that trajectories that approach from the 'N' end of the molecule can also impact on the 'O' end of the molecule. However, two peaks are not resolved in the angular range resolved DCS. This is because the two peaks in the DCS are at very similar scattering angles for 'N' end collisions due to the torque required for the rotational excitation. Collisions that impact on the 'N' end of the molecule result from higher impact parameter collisions and scatter through smaller angles than for corresponding 'O' end collisions, therefore it would be expected that the 'near end' peak would be shifted to smaller scattering angles and the 'far end' peak would be shifted to larger scattering angles. 'Far end' collisions that impact on the 'O' end of the molecule are not able to exert sufficient torque on the molecule to result in a $\Delta j = 10$ transition, and so only a single peak is seen in the 'N' end angular resolved DCS for this transition.

Although the normalized $R_1^{(1)}(\theta)$ moment does not contribute to the oriented DCS for this experimental geometry, as shown by Eq. (21), the calculated values of these r-PDDCSs are displayed on the bottom row of Fig. 8. The normalized $R_1^{(1)}(\theta)$ moment describes the orientation of the bond axis distribution relative to the scattering frame x axis, with positive values indicating an orientation in the $+x$ direction and negative values corresponding to preferred orientation antiparallel to the x axis. Unlike the $R_0^{(1)}(\theta)$ moment, $\Delta j = 3$ and $\Delta j = 15$ show opposite directional preferences, with low rotational excitation preferring collisions with the bond axis oriented parallel to the x-axis and high rotational excitation resulting from collisions with the bond axis oriented antiparallel to the x axis. This can be understood by considering the dynamics of collisions resulting in low and high rotational excitation. The secondary maxima in $\Delta j = 3$ is an ℓ-type rainbow, attributed to the build up of trajectories deflected to the far side of the molecule by the attractive part of the molecule resulting in a build up in scattering intensity at the rainbow angles. On the other

hand, high rotational excitation is a consequence of impulsive collisions that scatter to the near side of the molecule. These two situations are shown in panels c) and d) of Fig. 10. Since collisions towards the 'N' end of the molecule can exert more torque on the molecule, which is important both to induce high rotational excitation, and for high impact parameter collisions that result in ℓ-type rainbow scattering. In both situations, the collision occurs towards the 'N' end of the molecule, but as a consequence of the scattering to different sides of the molecule, the bond axis distribution is parallel to the x axis for deflection to the far side of the molecule and antiparallel for scattering to the near side of the molecule.

C. Quantum mechanical steric effect

The quantum mechanical calculations presented in this section were performed using the Hibridon[52] suite of codes at a collision energy of 530 cm^{-1}. The V_{sum} and V_{diff} coupled-cluster singles, doubles, perturbative triples (CCSD(T)) PESs of Alexander[49] were used, with the bond length of the NO(X) fixed at its equilibrium value. Rotational levels up to $j' = 20.5$, both Λ-doublet and spin-orbit levels were included in the calculations. Partial waves up to $J = 160.5$ were needed to achieve convergence, corresponding to a classical impact parameter of 6.8 Å.

For oriented NO(X), the scattering amplitude for a transition is given by[26,34]

$$f_{jmE\to j'm'\epsilon'}(\theta) = \frac{1}{\sqrt{2}}\left[\alpha f_{jme\to j'm'\epsilon'}(\theta) + \beta f_{jmf\to j'm'\epsilon'}(\theta)\right] , \tag{24}$$

where $f_{jm\epsilon\to j'm'\epsilon'}(\theta)$ is the scattering amplitude for the particular state-to-state transition at a scattering angle, θ and α and β are the mixing coefficients given in Eq. (5). The bond orientation resolved DCS is then calculated as the square modulus of the scattering amplitude.[26,49]

In previous studies of NO(X) + rare gas systems, it has been found that quantum interference makes a significant contribution to features in the differential cross sections[38] and collision induced rotational orientation.[53,54] The two top rows of Fig. 11 depict a comparison of QM and QCT calculated bond orientation resolved DCSs, with red lines indicating 'N' end collisions and blue lines indicating 'O' end collisions. The QM data shown are for spin-orbit conserving transitions, averaged over final Λ-doublet level for better comparison with the closed shell QCT calculations. There are a number of similarities between the QM and QCT

This manuscript was accepted by J. Chem. Phys. Click here to see the version of record.

DCSs, for example, the maximum in the DCS is found at increasingly large scattering angles as the rotational excitation increases. The effect of bond axis orientation is also very similar in the QM and QCT DCS for $\Delta j = 15$. As noted in Section I, at high Δj the integral and differential steric effects are well-accounted for by classical mechanics. However, for $\Delta j = 3$, the secondary maxima that is present in the QCT DCS is absent in the corresponding QM DCS, which is dominated by glory scattering, superimposed with rapid oscillations due to Fraunhofer diffraction.[50] As a result, the orientation of the NO bond axis has less of an effect on the QM DCS than for the QCT calculations. The effect of orientation on the DCSs for $\Delta j = 7$ and 10 transitions is also quite different for the QM and QCT calculations. The QCT DCSs for these middle Δj transitions show multiple peaks in the 'O' end DCSs for the reasons discussed in the previous section, whereas the number of peaks in the QM DCSs is the same for both orientations, with only the relative intensities of the peaks changing.

In order to investigate the differential steric asymmetry, it can also be convenient to consider the normalized difference DCS, $\mathrm{d}\sigma_{\mathrm{diff}}(\theta)$, which can be defined as[26]

$$\mathrm{d}\sigma_{\mathrm{diff}}(\theta) = \frac{\mathrm{d}\sigma_{\mathrm{N}}(\theta) - \mathrm{d}\sigma_{\mathrm{O}}(\theta)}{\mathrm{d}\sigma_{\mathrm{N}}(\theta) + \mathrm{d}\sigma_{\mathrm{O}}(\theta)} \,. \tag{25}$$

From Eq. (25) it can be seen that a positive value indicates an 'N' end preference for the scattering, and a negative value an 'O' end preference. Note that integration of Eq. (25), *i.e.* the integral of $\mathrm{d}\sigma_{\mathrm{diff}}(\theta)$ over θ, does not yield the integral steric asymmetry, which is defined by Eq. (1).[27]

Calculated $\mathrm{d}\sigma_{\mathrm{diff}}(\theta)$ normalized difference DCSs are shown in the bottom row of Fig. 11 for QM and QCT calculations. Significant differences between the QM and QCT normalized difference DCSs can be seen at low and medium rotational excitation. At $\Delta j = 3$, the QCT calculations show an 'N' end preference in the angular range of the ℓ-type rainbow, for the reasons discussed in Section IV B. Above approximately $\theta = 45°$, no steric preference is seen in the QCT calculations. Similarly, for $\Delta j = 7$, the QCT $\mathrm{d}\sigma_{\mathrm{diff}}(\theta)$ is zero above approximately $\theta = 55°$. In contrast, the QM calculated $\mathrm{d}\sigma_{\mathrm{diff}}(\theta)$ is non-zero and oscillatory throughout the entire angular range for both low and middle rotational excitation. For $\Delta j = 3$, no clear 'N' end preference in the region of the classical rainbow is seen in the QM calculations, which is hardly surprising given that no evidence of an ℓ-type rainbow can be seen in the QM DCS. Instead, $\mathrm{d}\sigma_{\mathrm{diff}}(\theta)$ oscillates very rapidly at low scattering angles for $\Delta j = 3$, indicating that bond axis orientation affects the form of the Fraunhofer diffraction

This manuscript was accepted by J. Chem. Phys. Click here to see the version of record.

oscillations. At high rotational excitation, the QM and QCT normalized difference DCSs are in reasonable agreement, indicating an 'N' end preference over all scattering angles, suggesting that the steric preference can be understood by the classical ball and stick model.

Despite the reasonable agreement between the QM and QCT calculated normalized difference DCSs at high rotational excitation, it is clear that for low and medium rotational excitation the steric preference of the NO(X) + Ar collision cannot be explained classically and must be quantum mechanical in origin.

In order gain a qualitative understanding of the oscillations in the QM normalized difference DCS, a semi-classical four path model has previously been used.[27,35,38,43] Within this model, the normalized difference DCS can be expressed as

$$\mathrm{d}\sigma_{\mathrm{diff}}(\theta) = \frac{4\alpha\beta\left(\cos\Delta\varphi_{\mathrm{N}} - \cos\Delta\varphi_{\mathrm{O}}\right)}{\mathrm{d}\sigma_{\mathrm{N}}^{\mathrm{fp}}(\theta) + \mathrm{d}\sigma_{\mathrm{O}}^{\mathrm{fp}}(\theta)}\,, \tag{26}$$

with

$$\begin{aligned}\mathrm{d}\sigma_{\mathrm{N}}^{\mathrm{fp}}(\theta) + \mathrm{d}\sigma_{\mathrm{O}}^{\mathrm{fp}}(\theta) = \alpha^2\left[6 + 4\left(\cos\Delta\varphi_{\mathrm{N}} + \cos\Delta\varphi_{\mathrm{O}}\right) + 2\cos\left(\Delta\varphi_{\mathrm{N}} - \Delta\varphi_{\mathrm{O}}\right)\right] \\ + 2\beta^2\left[1 - \cos\left(\Delta\varphi_{\mathrm{N}} - \Delta\varphi_{\mathrm{O}}\right)\right]\,.\end{aligned} \tag{27}$$

$\Delta\varphi_i$ is the phase shift associated with scattering from either end 'i' of the molecule compared with the flatter middle. Eq. (26) indicates that the differential steric asymmetry arises from a quantum interference between scattering from the two ends of the NO(X) molecule,[27] in agreement with the conclusions of the quasi-quantum treatment presented in Ref. 19. In the case of a homonuclear molecule $\Delta\varphi_{\mathrm{N}} = \Delta\varphi_{\mathrm{O}}$, and therefore $\mathrm{d}\sigma_{\mathrm{diff}}(\theta) = 0$ and no steric preference will be seen. This model has previously been used to rationalize the form of the normalized difference DCS for collisions of oriented NO with Ar.[27] Since this model only considers hard shell collisions, its success also suggests that the observed differential steric asymmetry is dominated by the repulsive region of the potential.

Fig. 12 shows QM calculated bond orientation resolved DCSs for spin-orbit conserving transitions to a final e Λ-doublet level performed on the full potential (top row) and on a soft repulsive potential, in which the attractive well has been removed[54,55] (middle row). The DCSs for both sets of calculations show the same general features and are in very good agreement at high rotational excitation (above $j' = 10.5$). However, at low and medium rotational excitation, the effect of the attractive region of the potential can be clearly seen, with the calculations performed on the full potential showing much more forwards scattering

than the calculations performed on the soft repulsive potential. For all rotational states, the peaks are shifted to slightly higher scattering angle for the soft repulsive calculations, although this effect decreases with increasing j', as the collisions will sample the more repulsive region of the full potential. The bottom row of Fig. 12 shows the normalized difference DCSs for the two sets of calculations. The same features are clearly observable in the calculations performed on both potentials, confirming the role of the repulsive region of the potential in determining the differential steric asymmetry. It can be seen that, in the soft repulsive calculations, the maxima and minima are shifted to slightly higher scattering angles than for the corresponding full potential calculations, due to the removal of the attractive region of the potential energy surface.

Previous investigations of the integral steric asymmetry[26] have shown that the final parity of the NO(X) does not significantly effect the observed integral steric asymmetry, which depends predominantly on final rotational state, j'. Fig. 13 shows the effect of final parity on the bond orientation resolved DCSs (top and middle rows) and normalized difference DCS (bottom row). At very low and high rotational excitation ($j' = 3.5$ and $j' = 15.5$), the DCSs for transitions to final e and f states are very similar. In contrast, for transitions to middle rotational states, clear differences can be seen in the bond orientation resolved DCSs for the e and f final states. It is perhaps surprising, therefore, that the normalized difference DCSs, $\mathrm{d}\sigma_{\mathrm{diff}}(\theta)$, for transitions to the two components of the Λ-doublet show very similar features for all transitions. The form of $\mathrm{d}\sigma_{\mathrm{diff}}(\theta)$ is therefore predominantly sensitive to the final j' state and not the parity of the final rotational wavefunction.

Future experimental and theoretical work will explore the differential steric asymmetry for spin-orbit changing collisions of NO + Ar, as well as for more complicated systems.

V. CONCLUSIONS

In this paper, a modification to the experimental apparatus to allow orientation of the NO bond axis prior to collisions has been designed and employed to measure bond orientation resolved differential cross sections for collisions of NO(X) with Ar. Simulations were performed to assess the effect of the orientation electrodes on the velocity mapping field, and calculate the electric field achievable, and the final design has been discussed. The orientation design described in this paper can be easily combined with conventional velocity

mgo ion imaging optics and therefore could be employed to study a variety of inelastic and reactive scattering systems.

Bond orientation resolved differential cross sections were presented in Section IV A and compared with QM calculations. Differences in the experimental DCSs for the two orientations were observed and were found to be in good agreement with the QM calculations.

Previous studies of the inelastic scattering of fully quantum state resolved NO by Ar have shown the DCSs to be highly sensitive to the change in parity on collisions.[38] To assess the effect of final parity in the current work, bond orientation resolved DCSs for transitions to $j' = n + 0.5, f$ and $j' = n - 0.5, e$ states were considered. In contrast to the unoriented case, the bond orientation resolved DCS and normalized difference DCS were found not to be significantly affected by the final parity, in agreement with previous investigation of the integral steric asymmetry. This is a consequence of the mixing of the initial parity, *i.e.* the mixing of the initial Λ-doublet levels, in the static field. This finding serves to illustrate the effect of the trade-off between parity and the selection of signed Ω, that is of reactant bond axis orientation.

The steric preference of NO(X) + Ar collisions has been investigated theoretically, employing classical and quantum mechanical calculations. The method for determining the QCT bond orientation resolved DCSs has been presented and the calculated r-PDDCSs and orientation resolved DCSs discussed. The features in the classical DCSs can be explained with reference to different types of scattering trajectory and the corresponding steric preference for such collisions. A comparison of QCT and QM orientation resolved DCSs and normalized difference DCSs showed that for low and middle j', the steric preference for NO(X) + Ar cannot be explained classically and is quantum mechanical in origin. A comparison of QM calculations performed using the full potential and purely repulsive potential has shown that the steric preference is dominated by the repulsive region of the potential; this is in contrast to the QCT calculations, where the influence of the attractive region of the potential was clear.

ACKNOWLEDGMENTS

The support of the UK EPSRC (to M.B. *via* Programme Grant EP/L005913/1), the EU (to M.B. *via* FP7 EU People ITN project 238671), and the Spanish Ministry of Science

and Innovation (grants CTQ2012-37404, CTQ2015-65033-P and CSD2009-00038, to F.J.A.) are gratefully acknowledged. S.S. acknowledges support from the National Basic Research Program of China (973 program) under grant No. 2013CB922200, and from the National Science Foundation of China under grant Nos. 11034003 and 91221301. S.D.S.G. and M.B. also thank Cambio Ltd. and Dr Peter Dean, in particular, for generous support. Associated data is deposited with the Oxford Research Archive.

REFERENCES

[1]F. J. Aoiz, M. Brouard, S. D. S. Gordon, B. Nichols, S. Stolte, and V. Walpole, Phys. Chem. Chem. Phys. **17**, 30210 (2015).

[2]R. J. Beuhler Jr, R. B. Bernstein, and K. H. Kramer, J. Am. Chem. Soc. **88**, 5331 (1966).

[3]R. J. Beuhler Jr and R. B. Bernstein, J. Chem. Phys. **51**, 5305 (1969).

[4]G. Marcelin and P. R. Brooks, J. Am. Chem. Soc. **95**, 7885 (1973).

[5]D. H. Parker, K. K. Chakravorty, and R. B. Bernstein, J. Phys. Chem. **85**, 466 (1981).

[6]D. H. Parker, K. K. Chakravorty, and R. B. Bernstein, Chem. Phys. Lett. **86**, 113 (1982).

[7]D. H. Parker and R. B. Bernstein, Ann. Rev. Phys. Chem. **40**, 561 (1989).

[8]H. J. Loesch and A. Remscheid, J. Chem. Phys. **93**, 4779 (1990).

[9]H. J. Loesch and J. Möller, J. Phys. Chem. A **101**, 7534 (1997).

[10]H. Loesch and J. Möller, Fara. Disc. **113**, 241 (1999).

[11]H. J. Loesch and F. Stienkemeier, J. Chem. Phys. **98**, 9570 (1993).

[12]F. J. Aoiz, M. T. Martínez, and V. Sáez-Rábanos, J. Chem. Phys. **114**, 8880 (2001).

[13]F. Wang, J. S. Lin, and K. Liu, Science **331**, 900 (2011).

[14]F. Wang, K. Liu, and T. P. Rakitzis, Nat. Chem. **4**, 636 (2012).

[15]F. Wang, J. S. Lin, and K. Liu, J. Chem. Phys. **140**, 084202 (2014).

[16]J. J. van Leuken, J. Bulthuis, S. Stolte, and J. G. Snijders, Chem. Phys. Lett. **260**, 595 (1996).

[17]M. J. L. de Lange, M. M. J. E. Drabbels, P. T. Griffiths, J. Bulthuis, S. Stolte, and J. G. Snijders, Chem. Phys. Lett. **313**, 491 (1999).

[18]M. J. L. de Lange, S. Stolte, C. A. Taatjes, J. Kłos, G. C. Groenenboom, and A. van der Avoird, J. Chem. Phys. **121**, 11691 (2004).

[19]A. Gijsbertsen, H. Linnartz, C. A. Taatjes, and S. Stolte, J. Am. Chem. Soc. **128**, 8777

(2006).

[20]C. A. Taatjes, A. Gijsbertsen, M. J. L. de Lange, and S. Stolte, J. Phys. Chem. A **111**, 7631 (2007).

[21]K. Schreel and J. J. ter Meulen, J. Phys. Chem. A **101**, 7639 (1997).

[22]M. C. van Beek, J. J. ter Meulen, and M. H. Alexander, J. Chem. Phys **113**, 637 (2000).

[23]R. Cireasa, A. Moise, and J. J. T. Meulen, J. Chem. Phys **123**, 064310 (2005).

[24]A. Moise, R. Cireasa, D. H. Parker, and J. J. ter Meulen, J. Chem. Phys. **125**, 204315 (2006).

[25]A. Moise, D. H. Parker, and J. J. ter Meulen, J. Chem. Phys. **126**, 124302 (2007).

[26]M. H. Alexander and S. Stolte, J. Chem. Phys. **112**, 8017 (2000).

[27]B. Nichols, H. Chadwick, S. D. S. Gordon, C. J. Eyles, B. Hornung, M. Brouard, M. H. Alexander, F. J. Aoiz, A. Gijsbertsen, and S. Stolte, Chem. Sci. **6**, 2202 (2015).

[28]D. H. Parker and A. T. J. B. Eppink, J. Chem. Phys. **107**, 2357 (1997).

[29]D. W. Chandler and P. L. Houston, J. Chem. Phys. **87**, 1445 (1987).

[30]M. L. Lipciuc, A. J. van den Brom, L. Dinu, and M. H. M. Janssen, Rev. Sci. Instrum. **76**, 123103 (2005).

[31]M. H. Alexander, J. Chem. Phys. **76**, 5974 (1982).

[32]M. H. Alexander, Chem. Phys. **92**, 337 (1985).

[33]M. G. Tenner, E. W. Kuipers, W. Y. Langhout, A. W. Kleyn, G. Nicolasen, and S. Stolte, Surface Science **236**, 151 (1990).

[34]M. H. Alexander, Faraday Discussions **113**, 437 (1999).

[35]C. J. Eyles, M. Brouard, H. Chadwick, B. Hornung, B. Nichols, C. H. Yang, J. Kłos, F. J. Aoiz, A. Gijsbertsen, A. E. Wiskerke, and S. Stolte, Phys. Chem. Chem. Phys. **14**, 5403 (2012).

[36]M. Brouard, H. Chadwick, C. J. Eyles, B. Hornung, B. Nichols, J. M. Scott, F. J. Aoiz, J. Kos, S. Stolte, and X. Zhang, Mol. Phys. **111**, 1759 (2013).

[37]M. Brouard, H. Chadwick, S. D. S. Gordon, B. Hornung, B. Nichols, J. Kłos, F. J. Aoiz, and S. Stolte, J. Chem. Phys. **141**, 164306 (2014).

[38]C. J. Eyles, M. Brouard, C. H. Yang, J. Kłos, F. J. Aoiz, A. Gijsbertsen, A. E. Wiskerke, and S. Stolte, Nat. Chem. **3**, 597 (2011).

[39]SIMION 8.1, "`http://simion.com/`,".

[40]A. von Zastrow, J. Onvlee, S. N. Vogels, G. C. Groenenboom, A. van der Avoird, and

S. Y. T. van de Meerakker, Nat. Chem. **6**, 216 (2014).

[41]A. Gijsbertsen, H. Linnartz, G. Rus, A. E. Wiskerke, S. Stolte, D. W. Chandler, and J. Kłos, J. Chem. Phys. **123**, 224305 (2005).

[42]F. J. Aoiz, J. E. Verdasco, M. Brouard, J. Kłos, S. Marinakis, and S. Stolte, J. Phys. Chem. A **113**, 14636 (2009).

[43]C. J. Eyles, M. Brouard, H. Chadwick, F. J. Aoiz, J. Kłos, A. Gijsbertsen, X. Zhang, and S. Stolte, Phys. Chem. Chem. Phys. **14**, 5420 (2012).

[44]A. Ballast, A. Gijsbertsen, H. Linnartz, and S. Stolte, Mol. Phys. **106**, 315 (2008).

[45]J. Aldegunde, M. P. de Miranda, J. M. Haigh, B. K. Kendrick, V. Sáez-Rábanos, and F. J. Aoiz, J. Phys. Chem. A **109**, 6200 (2005).

[46]J. Aldegunde, P. G. Jambrina, V. Sáez-Rábanos, M. P. de Miranda, and F. J. Aoiz, Phys. Chem. Chem. Phys. **12**, 13626 (2010).

[47]M. P. de Miranda, F. J. Aoiz, L. Bañares, and V. Sáez-Rábanos, J. Chem. Phys. **111** (1999).

[48]A. J. Orr-Ewing and R. N. Zare, Ann. Rev. Phys. Chem. **45**, 315 (1994).

[49]M. H. Alexander, J. Chem. Phys. **111**, 7426 (1999).

[50]H. Chadwick, B. Nichols, S. D. S. Gordon, B. Hornung, E. Squires, M. Brouard, J. Kłos, M. H. Alexander, F. J. Aoiz, and S. Stolte, J. Phys. Chem. Lett. **5**, 3296 (2014).

[51]F. J. Aoiz, J. E. Verdasco, V. J. Herrero, V. Sáez-Rábanos, and M. H. Alexander, J. Chem. Phys. **119**, 5860 (2003).

[52]HIBRIDON is a package of programs for the time-independent quantum treatment of inelastic collisions and photodissociation written by M. H. Alexander, D. Manolopoulos, H. J. Werner, and B. Follmeg, with contributions by P. F. Vohralik, D. Lemoine, G. Corey, R. Gordon, B. Johnson, T. Orlikowski, A. Berning, A. D. Esposti, C. Rist, P. Dagdigian, B. Pouilly, G. van der Sanden, M. Yang, F. de Weerd, S. Gregurick, and J. Kłos.

[53]J. I. Cline, K. T. Lorenz, E. A. Wade, J. W. Barr, and D. W. Chandler, J. Chem. Phys. **115**, 6277 (2001).

[54]M. Brouard, H. Chadwick, S. D. S. Gordon, B. Hornung, B. Nichols, F. J. Aoiz, and S. Stolte, J. Phys. Chem. A **119**, 12404 (2015).

[55]M. Brouard, H. Chadwick, C. J. Eyles, B. Hornung, B. Nichols, F. J. Aoiz, P. G. Jambrina, S. Stolte, and M. P. de Miranda, J. Chem. Phys. **138**, 104309 (2013).

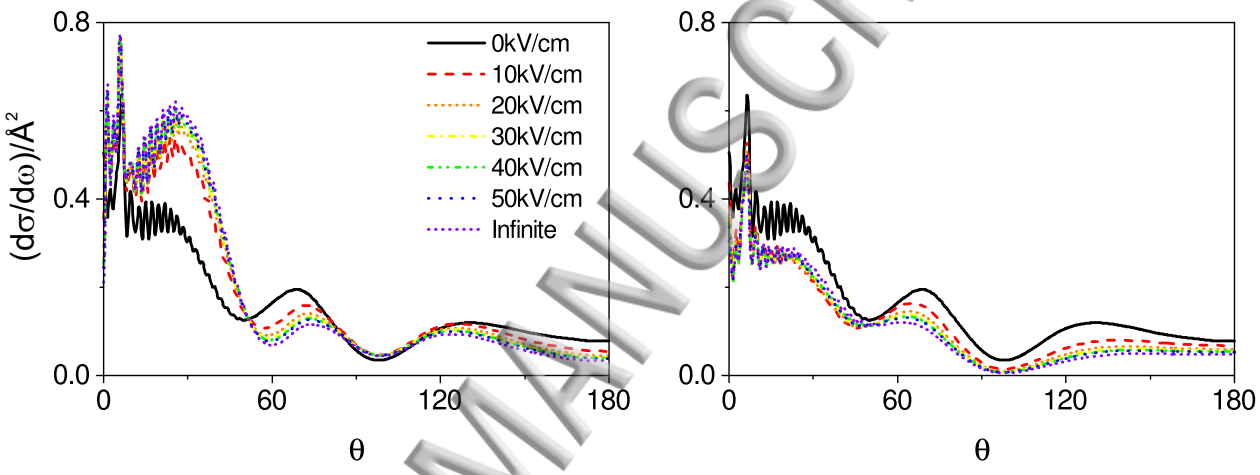

FIG. 1. Quantum mechanical calculated bond orientation resolved DCSs for collisions of NO(X) with Ar resulting in a transition to the $|\Omega' = 0.5, j' = 7.5, e\rangle$ state. DCSs for collisions with the 'N' end of the molecule are shown in the left panel and 'O' end in the right panel. DCSs for unoriented collisions (0 kV cm) are indicated by the black line. Calculations for a range of different field strengths are shown by the coloured lines.

This manuscript was accepted by J. Chem. Phys. Click here to see the version of record.

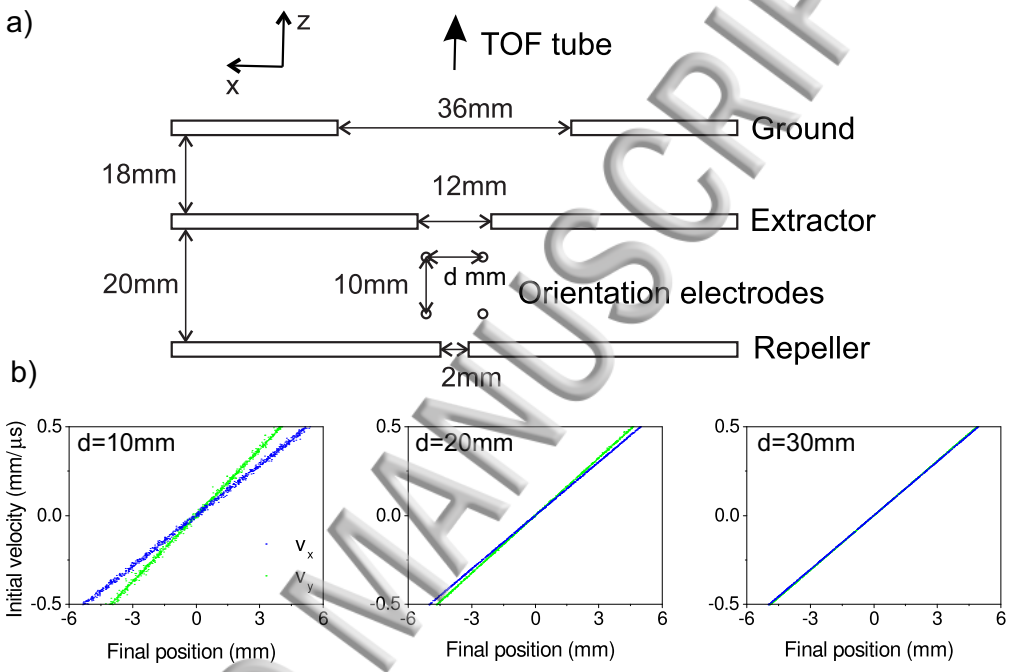

FIG. 2. Panel (a): schematic of the velocity map imaging electrodes used in the experimental apparatus. The thickness of the electrodes and rods was 1 mm. During simulations, the horizontal distance between the orientation electrodes, d, is varied, keeping the vertical separation fixed at 10 mm. Panel (b): plot of the x and y components of the initial velocity against the final position on the detector for orientation electrode spacings of 10 mm (left panel), 20 mm (middle panel) and 30 mm (right panel). All plots show an R^2 correlation coefficient above 0.999.

This manuscript was accepted by J. Chem. Phys. Click here to see the version of record.

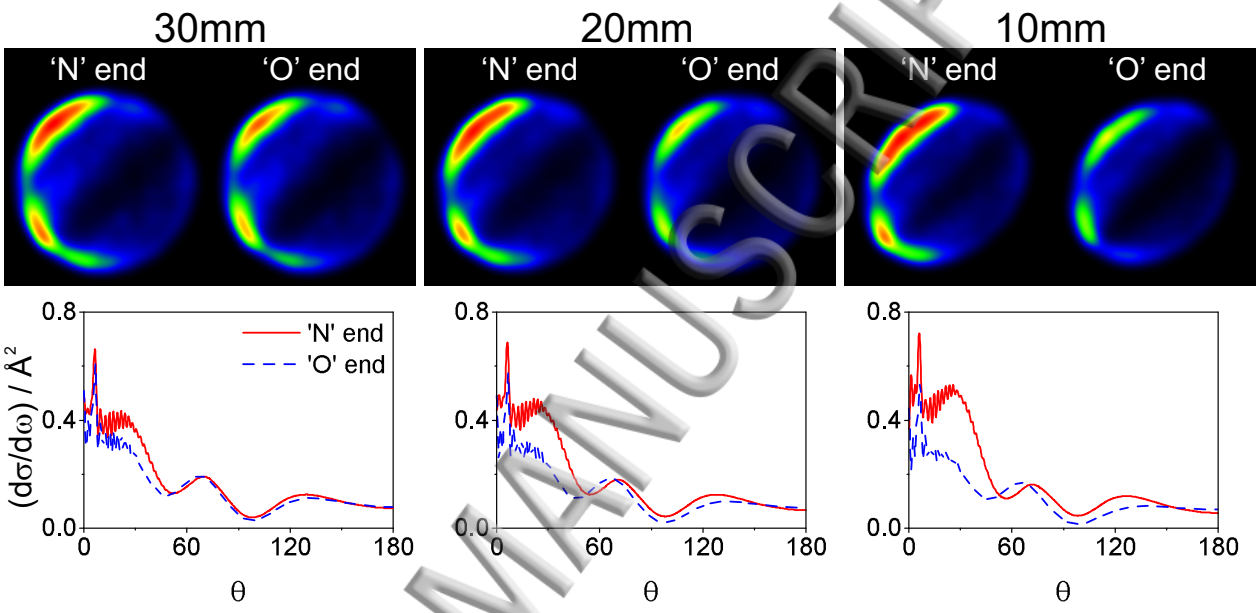

FIG. 3. QM calculated differential cross sections for 'N' (red continuous line) and 'O' (blue dashed line) end collisions resulting in a final state $|\Omega = 0.5, j' = 7.5, e\rangle$ for field strengths corresponding to orientation electrode spacings of 10 mm, 20 mm and 30 mm. The electric field used for the simulations were 9.2 kV cm^{-1}, 4.5 kV cm^{-1}, 2.0 kV cm^{-1} for 10 mm, 20 mm and 30 mm, respectively. The fields correspond to applying ±8 kV to the rods in each case. Corresponding simulated images are displayed in the top row. The distortion of the circularity of the image is calculated from SIMION simulations.

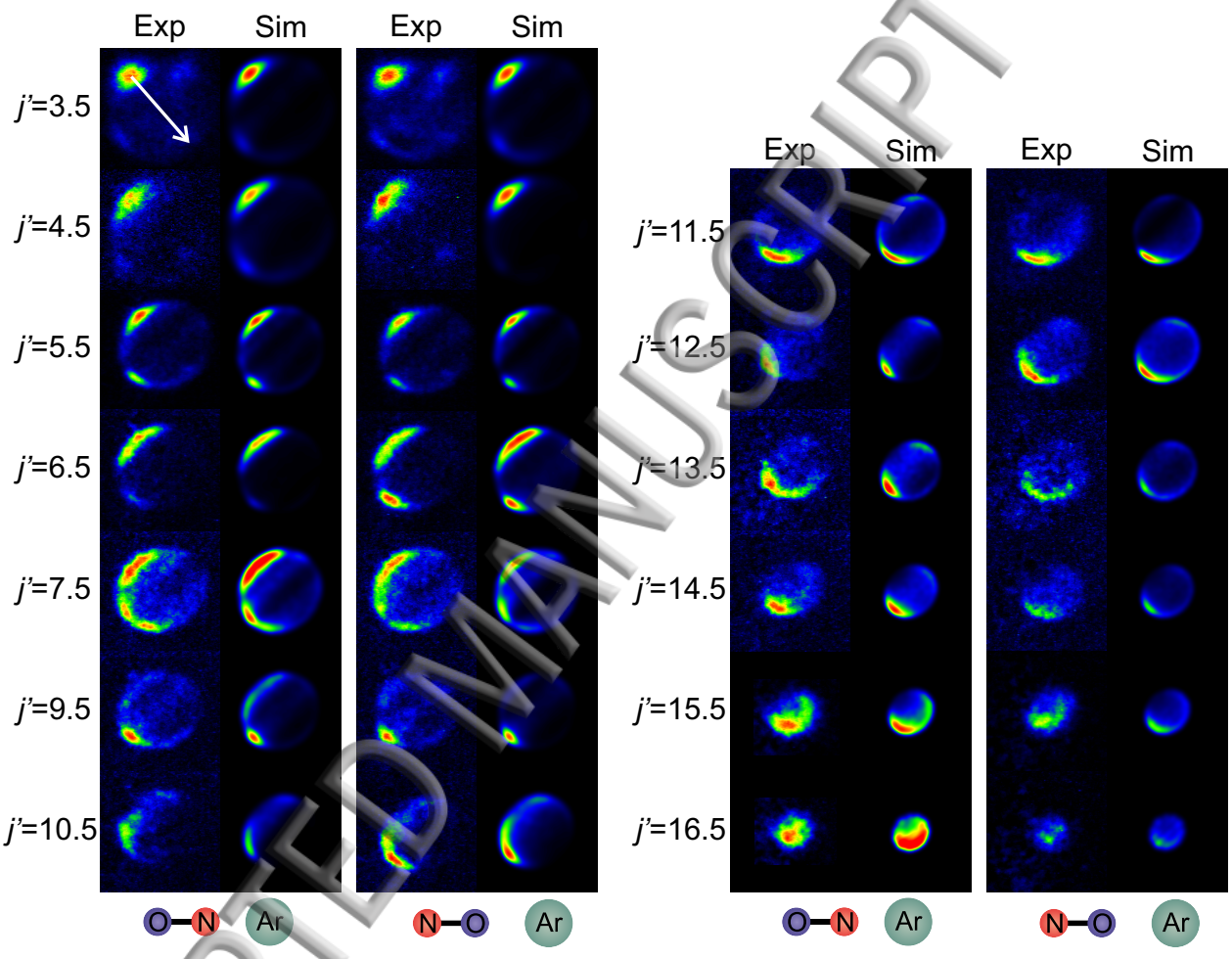

FIG. 4. Experimental and QM simulated ion images for spin-orbit conserving transitions into the e Λ-doublet level. The first and third columns shows images for 'N' end collisions whilst 'O' end images are displayed in the second and fourth columns. The white arrow in the top left panel indicates the direction of the relative velocity.[27]

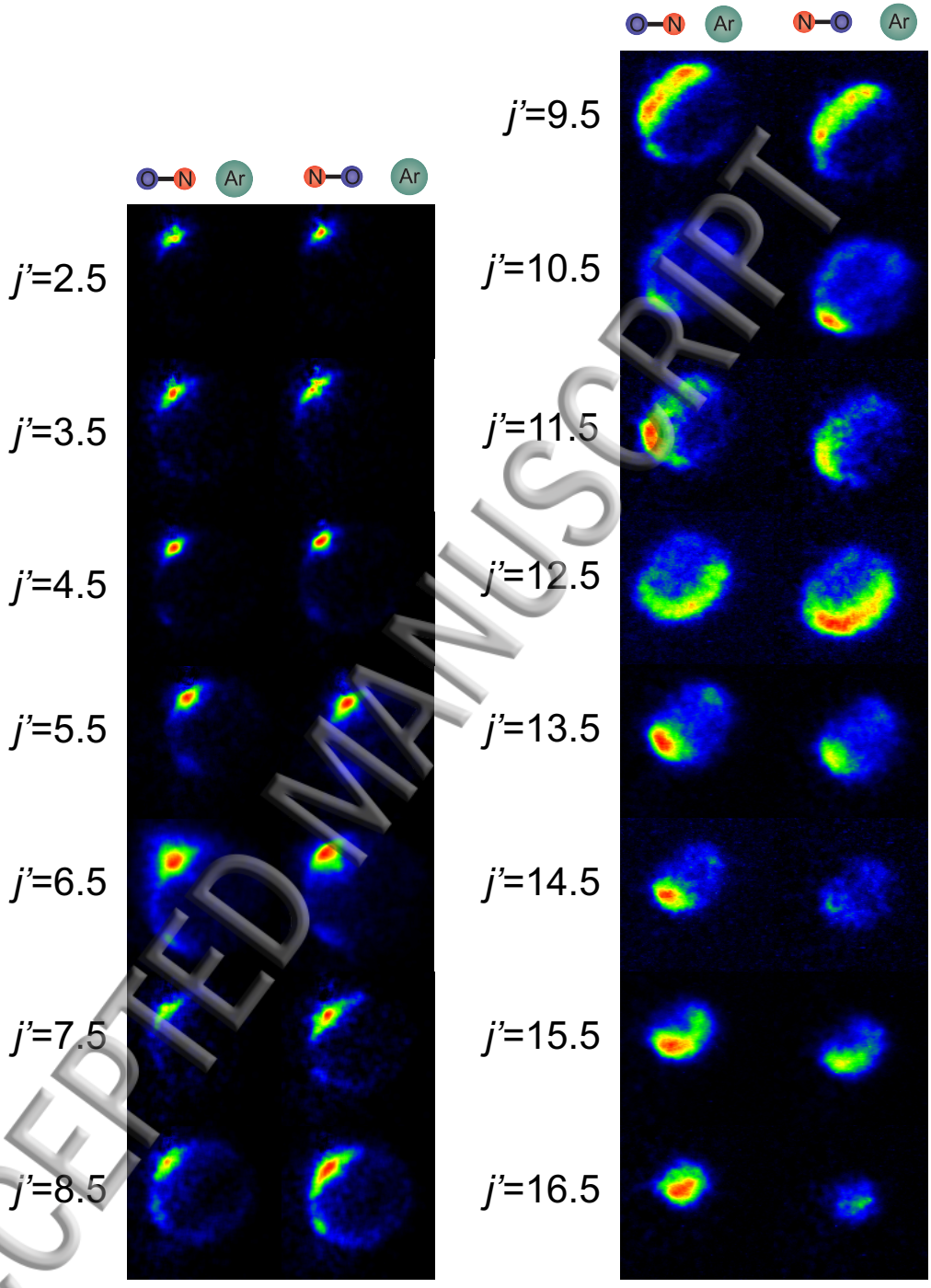

FIG. 5. Experimental ion images for spin-orbit conserving transitions into the f Λ-doublet level. The first and third columns shows images for 'N' end collisions whilst 'O' end images are displayed in the second and fourth columns.

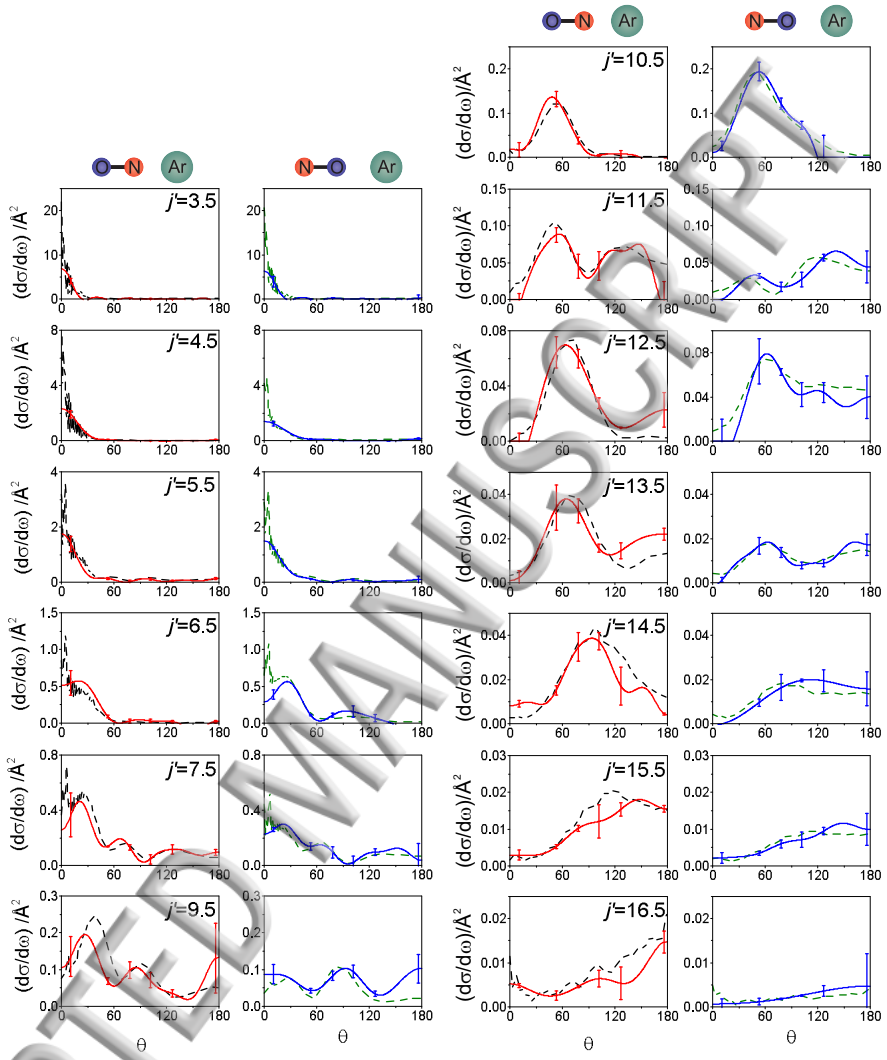

FIG. 6. Experimentally determined DCSs (red and blue continuous lines) for collisions of oriented NO(X) with Ar compared with corresponding QM calculated DCSs (black and green dashed lines) for spin-orbit conserving collisions into the e Λ-doublet level. DCSs corresponding to 'N' end collisions are shown in the first and third columns (red line), with 'O' end DCSs displayed in the second and fourth columns (blue line). The error bars associated with the experimental data represent the 95% confidence limits.

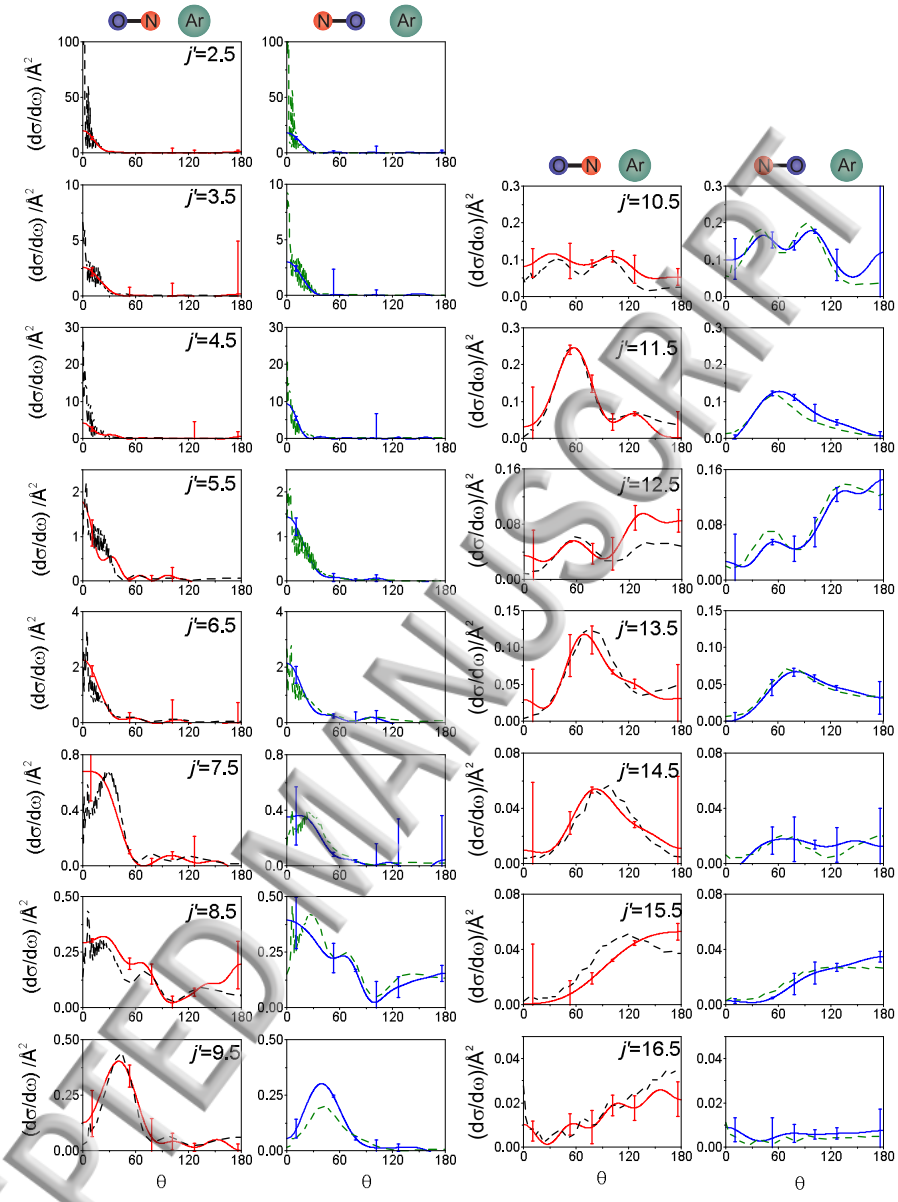

FIG. 7. Experimentally determined DCSs (red and blue continuous lines) for collisions of oriented NO(X) with Ar compared with corresponding QM calculated DCSs (black and green dashed lines) for spin-orbit conserving collisions into the f Λ-doublet level. DCSs corresponding to 'N' end collisions are shown in the first and third columns (red line), with 'O' end DCSs displayed in the second and fourth columns (blue line). The error bars associated with the experimental data represent the 95% confidence limits.

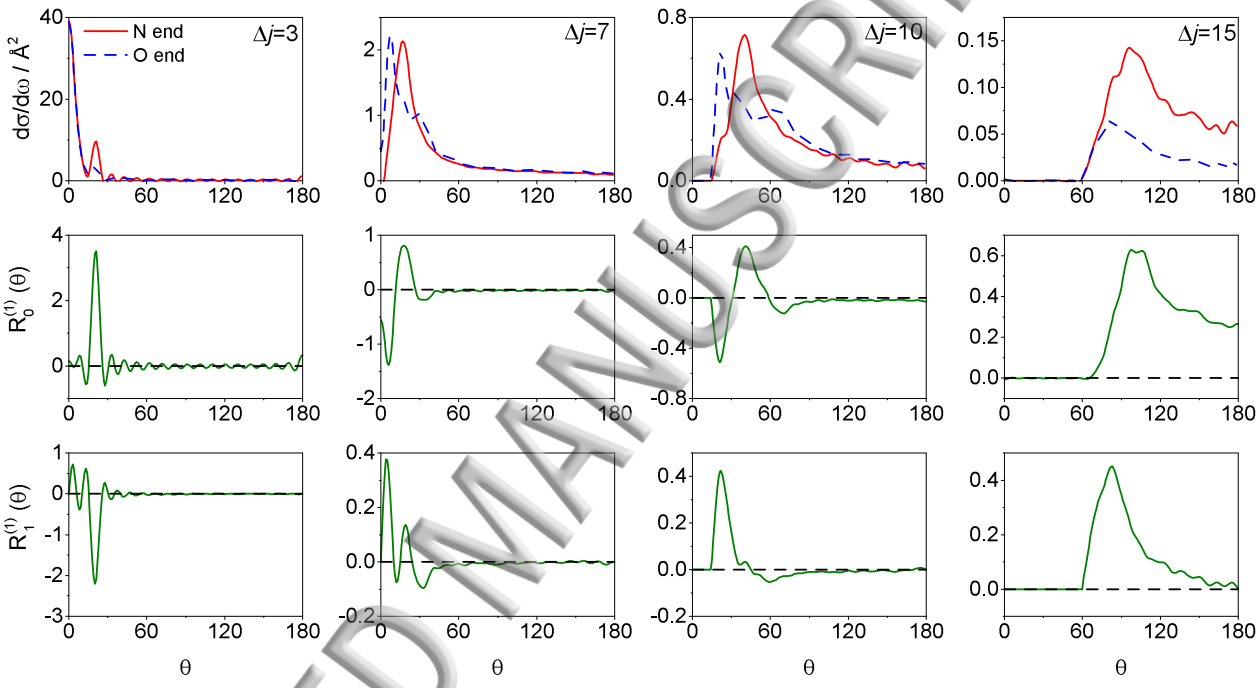

FIG. 8. QCT DCSs calculated for 'N' (red continuous line) and 'O' (blue dashed line) end collisions of NO(X) with Ar for $\Delta j = 3$ (first column), $\Delta j = 7$ (second column), $\Delta j = 10$ (third column) and $\Delta j = 15$ (fourth column) transitions. The corresponding $R_0^{(1)}(\theta)$ normalized r-PDDCSs used in the calculations are shown in the middle row and the $R_1^{(1)}(\theta)$ r-PDDCSs in the bottom row.

This manuscript was accepted by J. Chem. Phys. Click here to see the version of record.

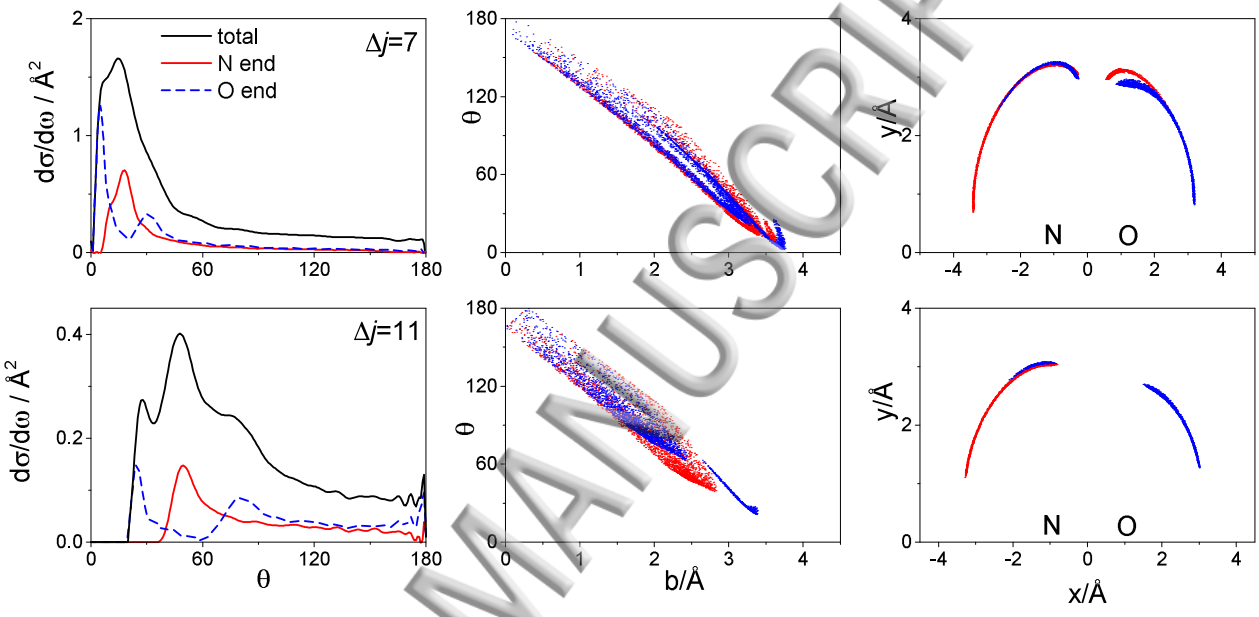

FIG. 9. QCT DCSs for non-oriented reagents in NO(X) + Ar collision with $\Delta j = 7$ (top panels) and $\Delta j = 11$ (bottom panels). Black continuous lines: DCS for the whole range of θ_r ($0° \leq \theta_r \leq 180°$). Red continuous lines: DCS for collisions in the $0° \leq \theta_r \leq 45°$ range, corresponding to 'N' end collisions. Blue dashed lines: DCS for collisions $135° \leq \theta_r \leq 180°$, corresponding to 'O' end collisions. Deflection functions for the $0° \leq \theta_r \leq 45°$ (red) and $135° \leq \theta_r \leq 180°$ (blue) ranges are shown in the middle column. Plots of the distance of closest approach in Cartesian coordinates for the two transitions are shown in the third column.

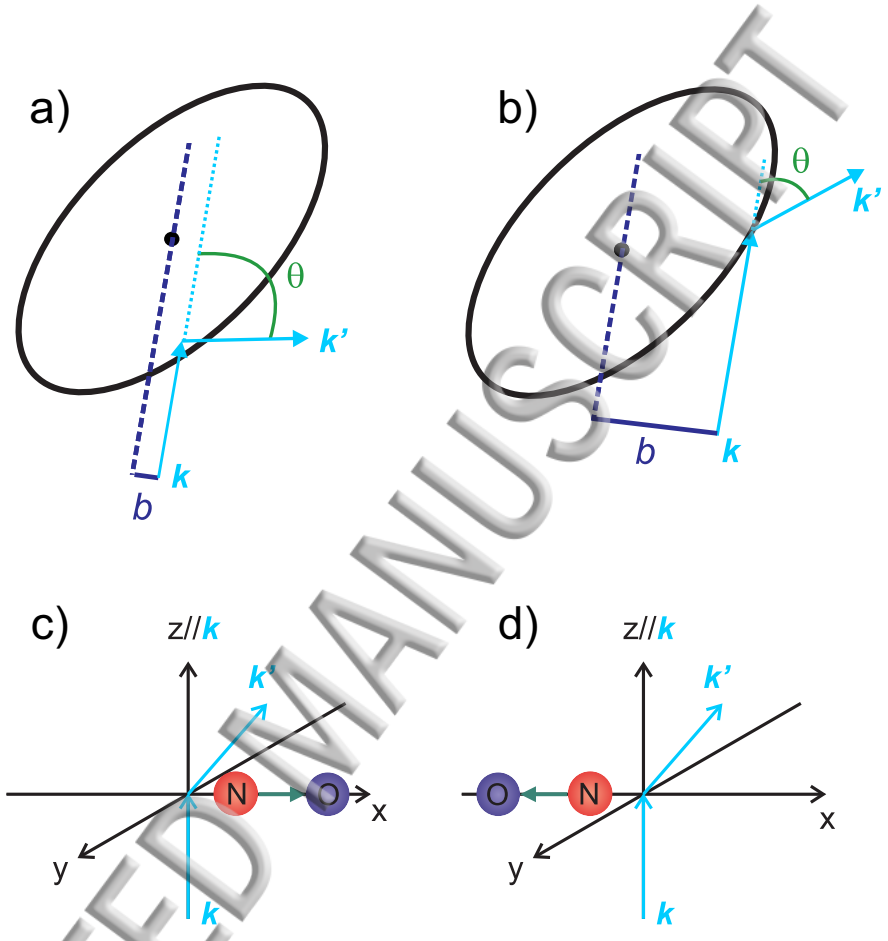

FIG. 10. Panels (a) and (b): Depiction of small (left panel) and large (right panel) impact parameter collisions leading to 'near' and 'far' end collisions respectively. Panels (c) and (d): Depiction of preferred bond axis orientation with respect to the scattering frame x axis for 'ℓ'-type rainbow scattering (panel c) resulting in low rotational excitation and impulsive scattering leading to high rotational excitation (panel d).

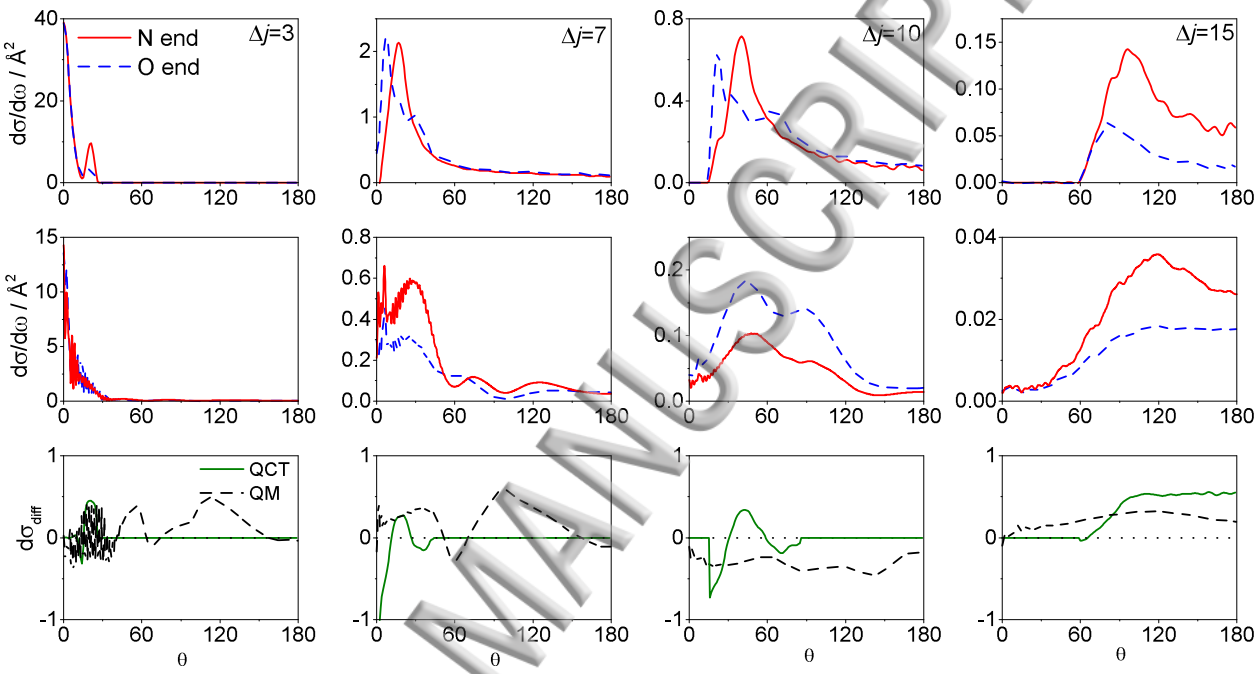

FIG. 11. Comparison of bond orientation resolved DCSs for closed shell QCT (top row) and Λ-doublet averaged open-shell QM (middle row) calculations for $\Delta j = 3$ (first column), $\Delta j = 7$ (second column), $\Delta j = 10$ (third column) and $\Delta j = 15$ (fourth column). In the top two rows 'N' end collisions are indicated by red continuous lines, whilst blue dashed lines show 'O' end collisions. The QM data are for spin-orbit conserving transitions, averaged over final e and f Λ-doublet levels. In the bottom row, a comparison of the normalized difference DCSs, $\mathrm{d}\sigma_{\mathrm{diff}}(\theta)$, for the QM (black dashed line) and QCT (green continuous line) calculations is shown.

This manuscript was accepted by J. Chem. Phys. Click here to see the version of record.

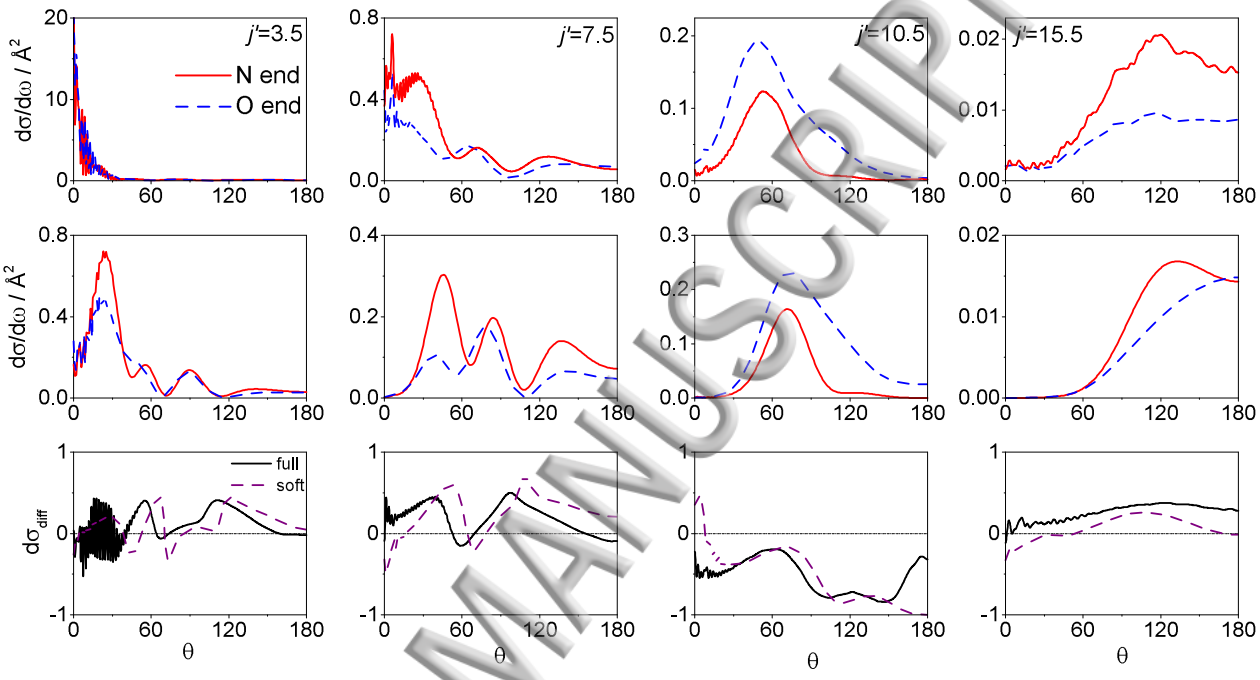

FIG. 12. Comparison of bond orientation resolved DCSs for open-shell QM calculations performed on the full (top row) and soft repulsive (middle row) potential energy surfaces for $\Delta j = 3$ (first column), $\Delta j = 7$ (second column), $\Delta j = 10$ (third column) and $\Delta j = 15$ (fourth column). 'N' end collisions are indicated by red continuous lines, whilst blue dashed lines show 'O' end collisions. The bottom row shows a comparison of the normalized difference DCSs, $\mathrm{d}\sigma_{\mathrm{diff}}(\theta)$, for QM calculations performed on the full potential (black continuous line), on the soft repulsive potential (magenta dashed line). The calculations are performed for spin-orbit conserving transitions to a final e Λ-doublet level.

This manuscript was accepted by J. Chem. Phys. Click here to see the version of record.

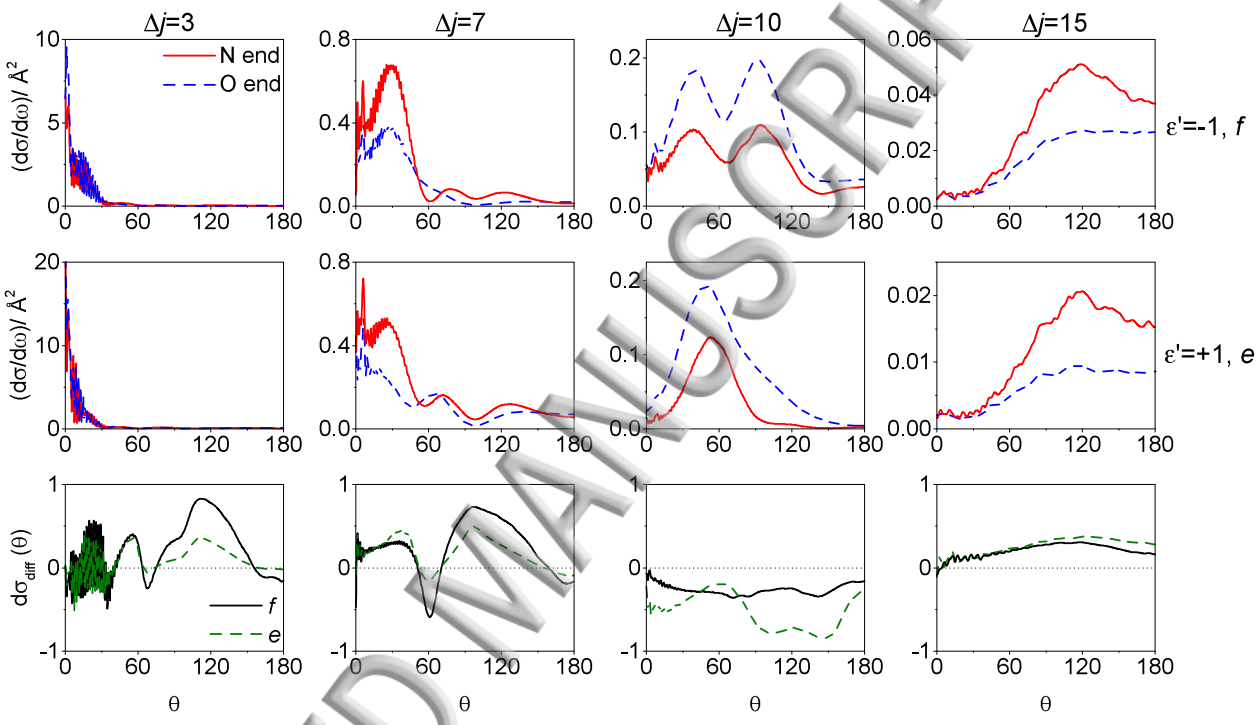

FIG. 13. Comparison of QM calculated bond orientation resolved DCSs for spin-orbit conserving transitions to final f (top row) and e (middle row) Λ-doublet levels. 'N' end collisions are indicated by red continuous lines, whilst blue dashed lines show 'O' end collisions. The bottom row shows normalized difference DCSs, $d\sigma_{diff}(\theta)$, for collisions resulting in final f (black continuous line) and e (green dashed line) levels.

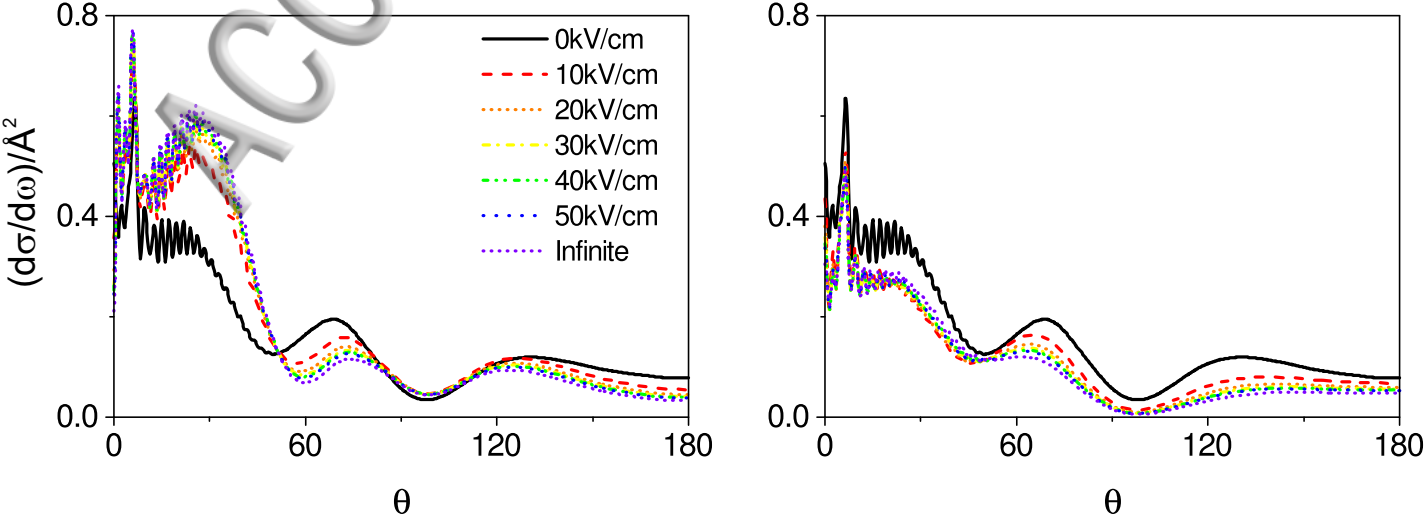
0.8
0.4
0.0
(dσ/dω)/Å²
0
60
120
180
θ
0kV/cm
10kV/cm
20kV/cm
30kV/cm
40kV/cm
50kV/cm
Infinite
0.8
0.4
0.0
0
60
120
180
θ

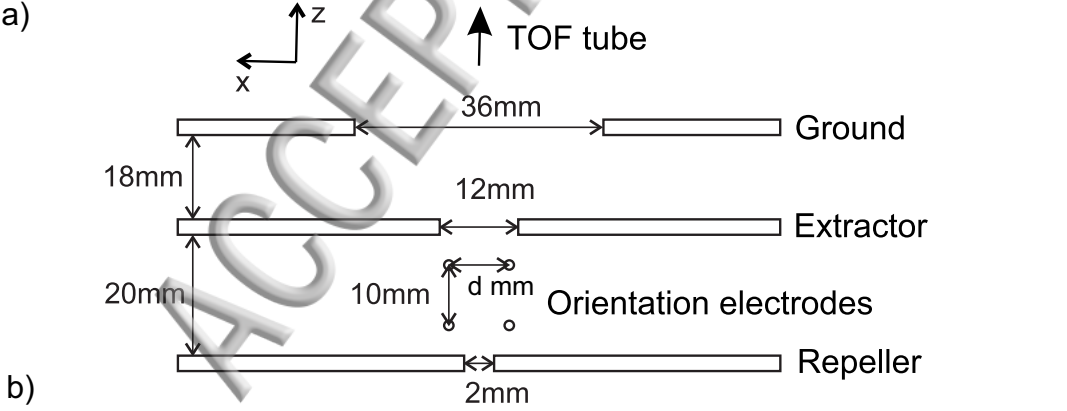
a)
z
x
TOF tube
36mm
Ground
18mm
12mm
Extractor
20mm
10mm
d mm
Orientation electrodes
Repeller
2mm
b)
d=10mm
d=20mm
d=30mm
Initial velocity (mm/μs)
0.5
0.0
-0.5
-6
-3
0
3
6
v_x
v_y
Final position (mm)

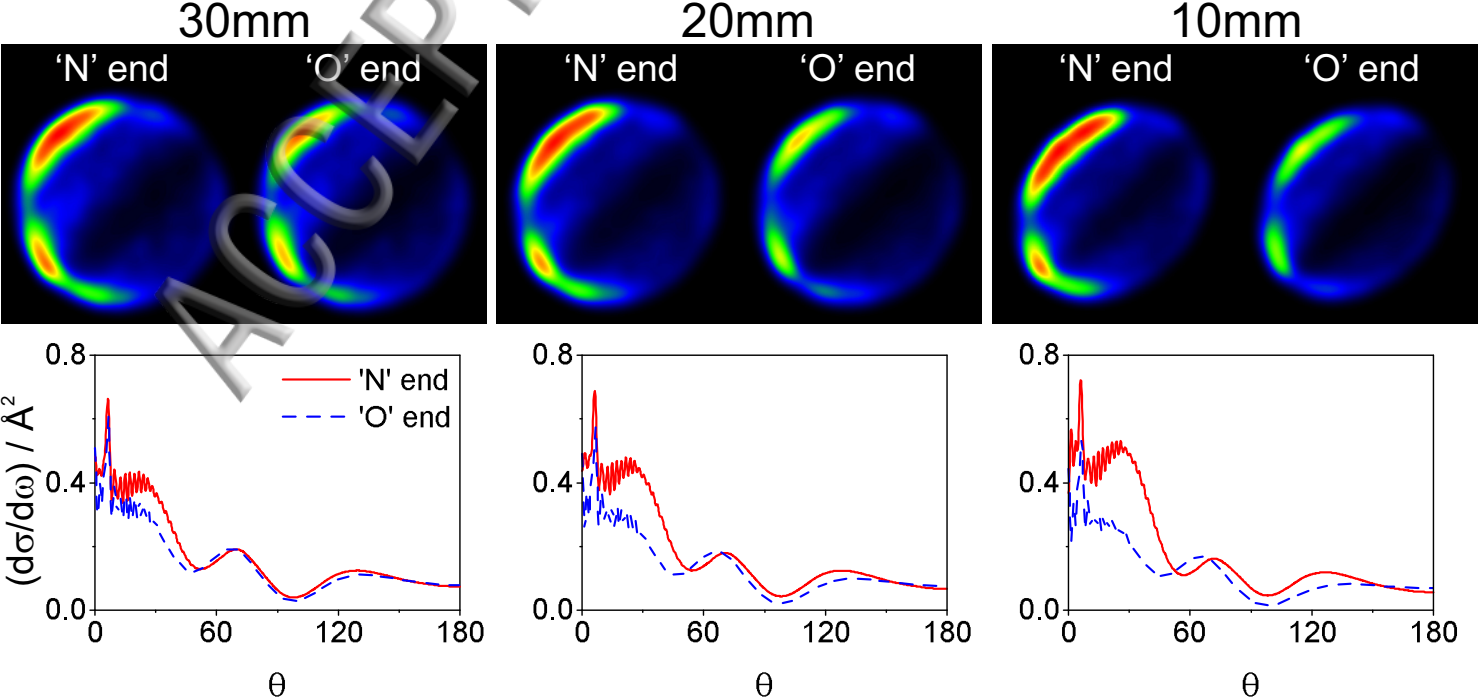
30mm
20mm
10mm
'N' end
'O' end
'N' end
'O' end
'N' end
'O' end
'N' end
'O' end
'N' end
'O' end
(dσ/dω) / Å²
0.8
0.4
0.0
0
60
120
180
θ

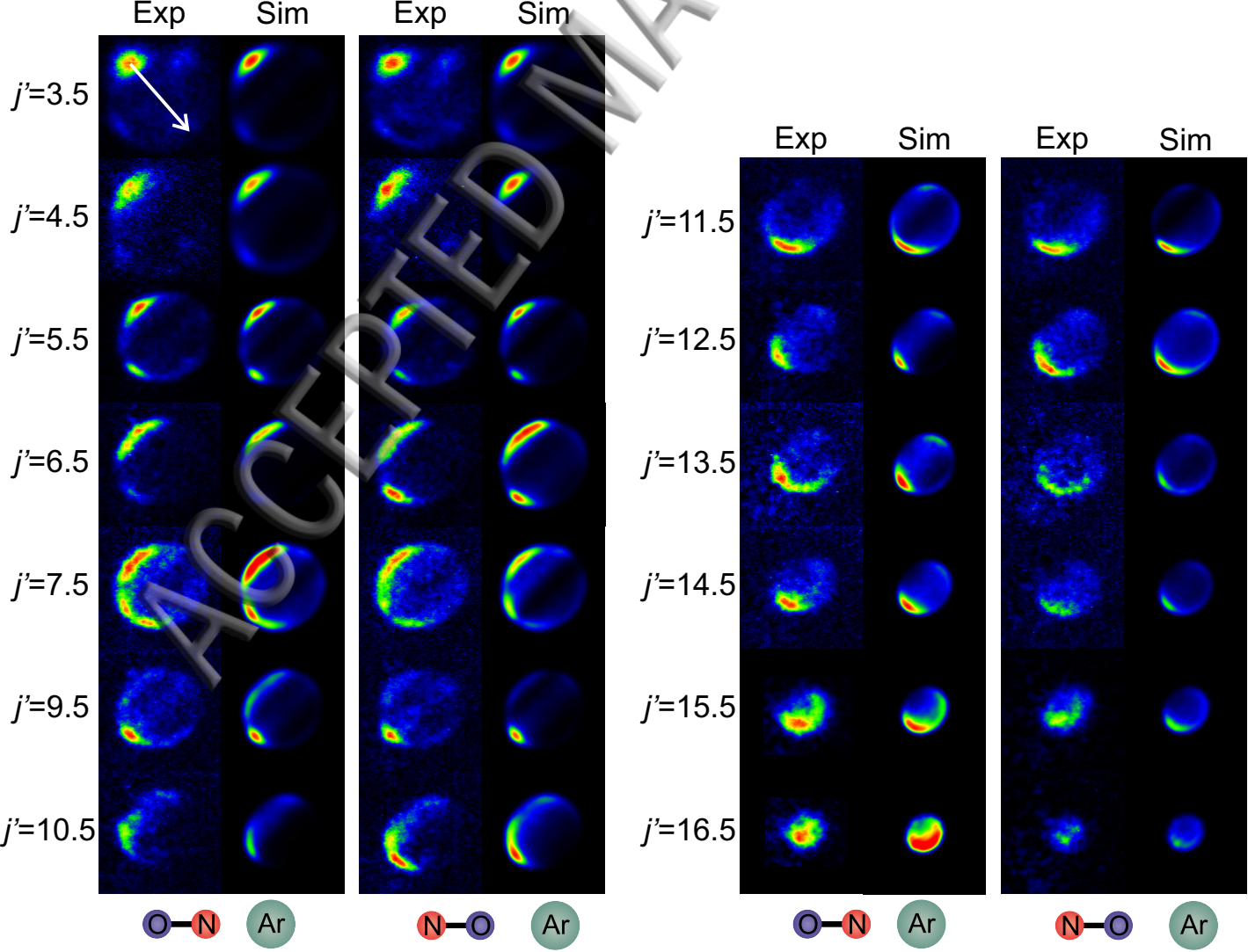
Exp
Sim
Exp
Sim
j'=3.5
j'=4.5
j'=5.5
j'=6.5
j'=7.5
j'=9.5
j'=10.5
O
N
Ar
N
O
Ar
Exp
Sim
Exp
Sim
j'=11.5
j'=12.5
j'=13.5
j'=14.5
j'=15.5
j'=16.5
O
N
Ar
N
O
Ar

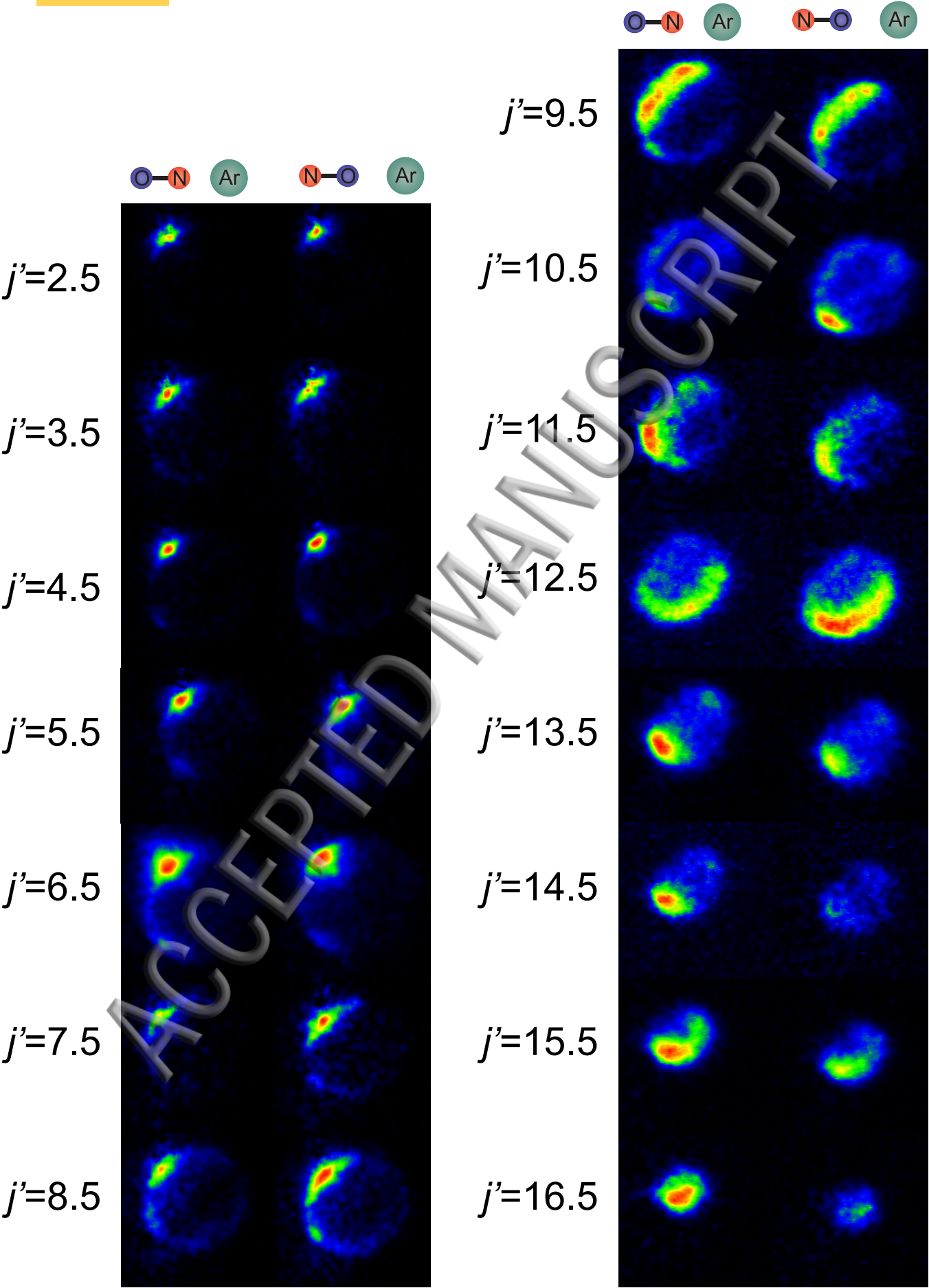

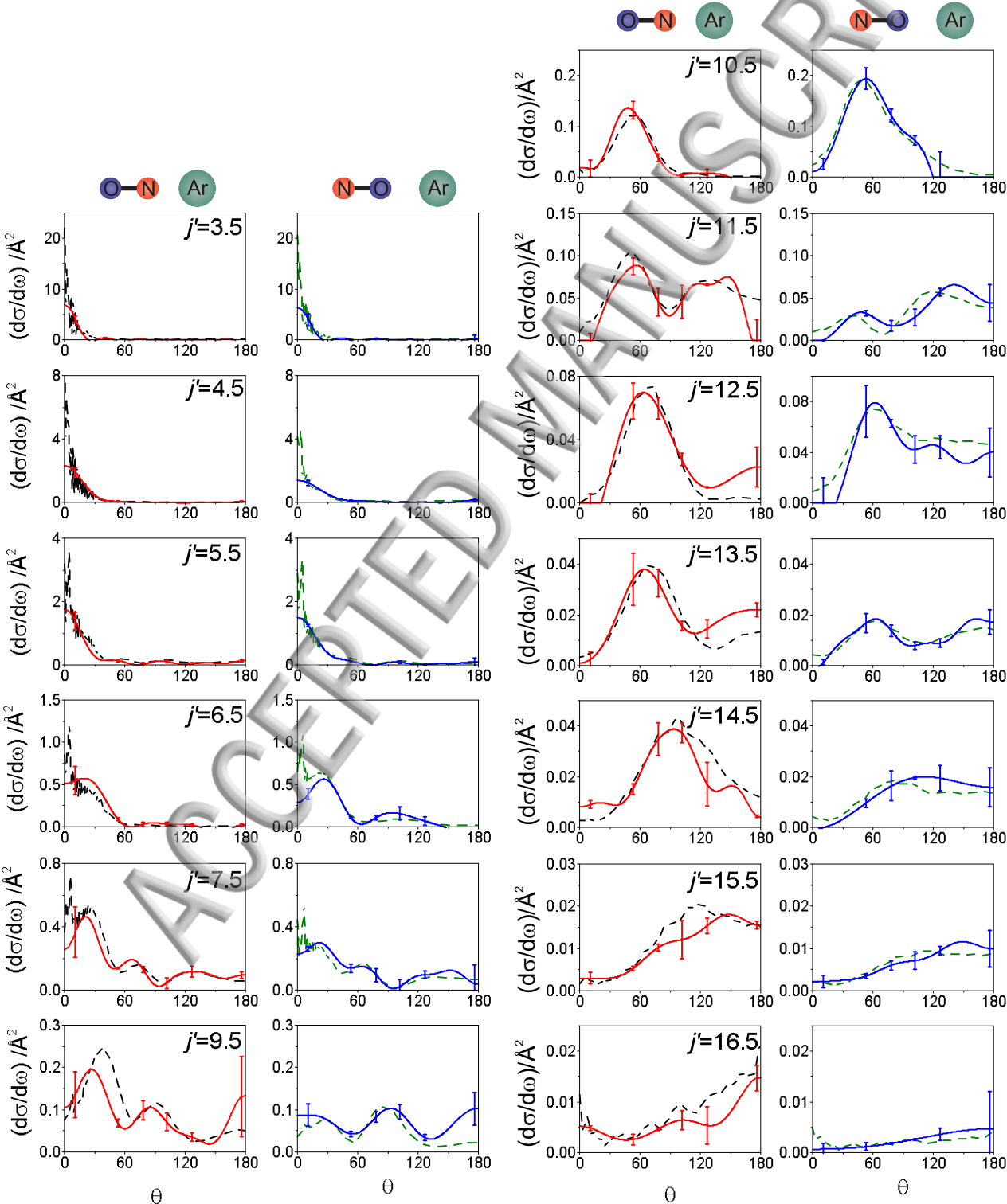

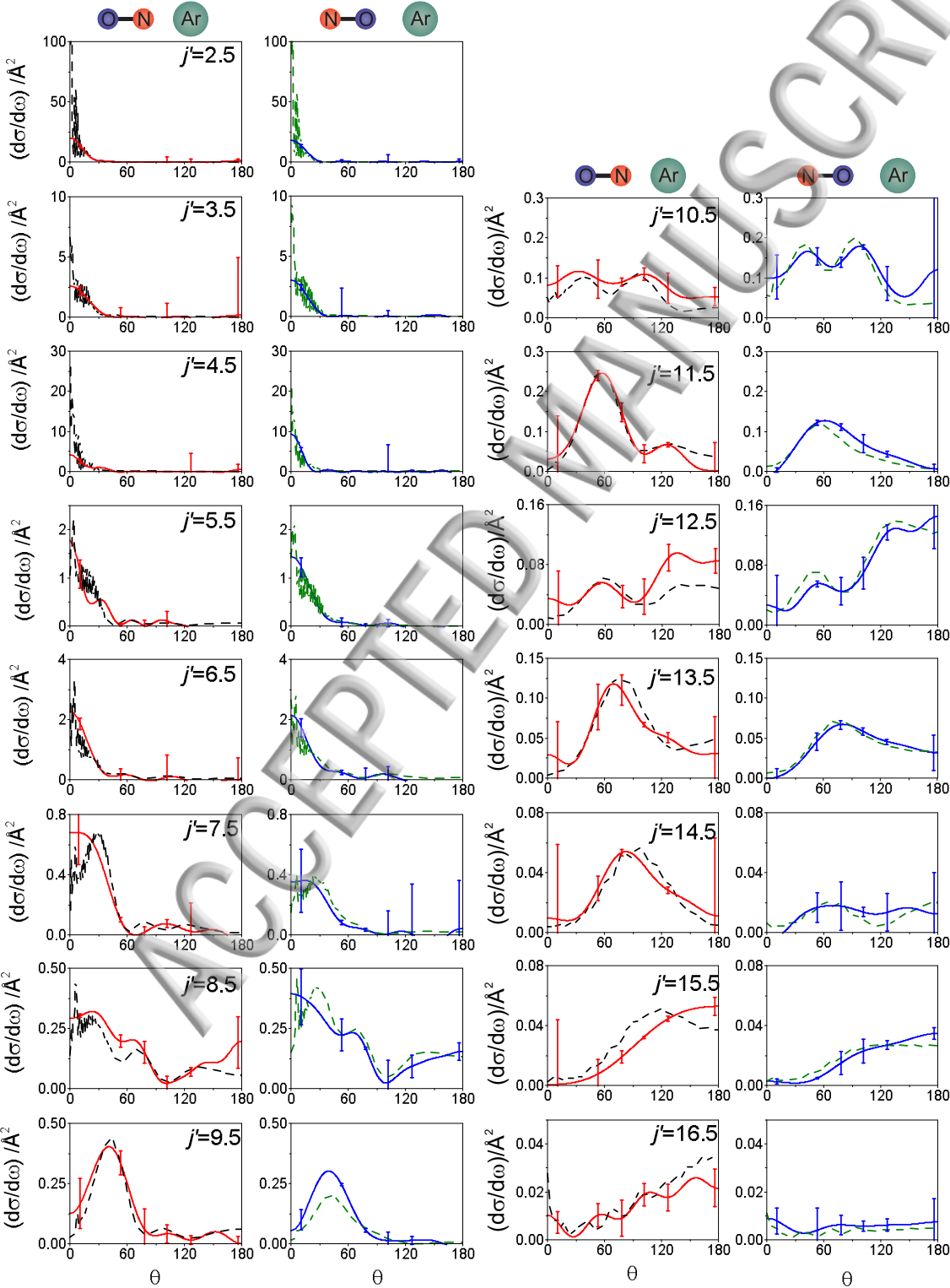

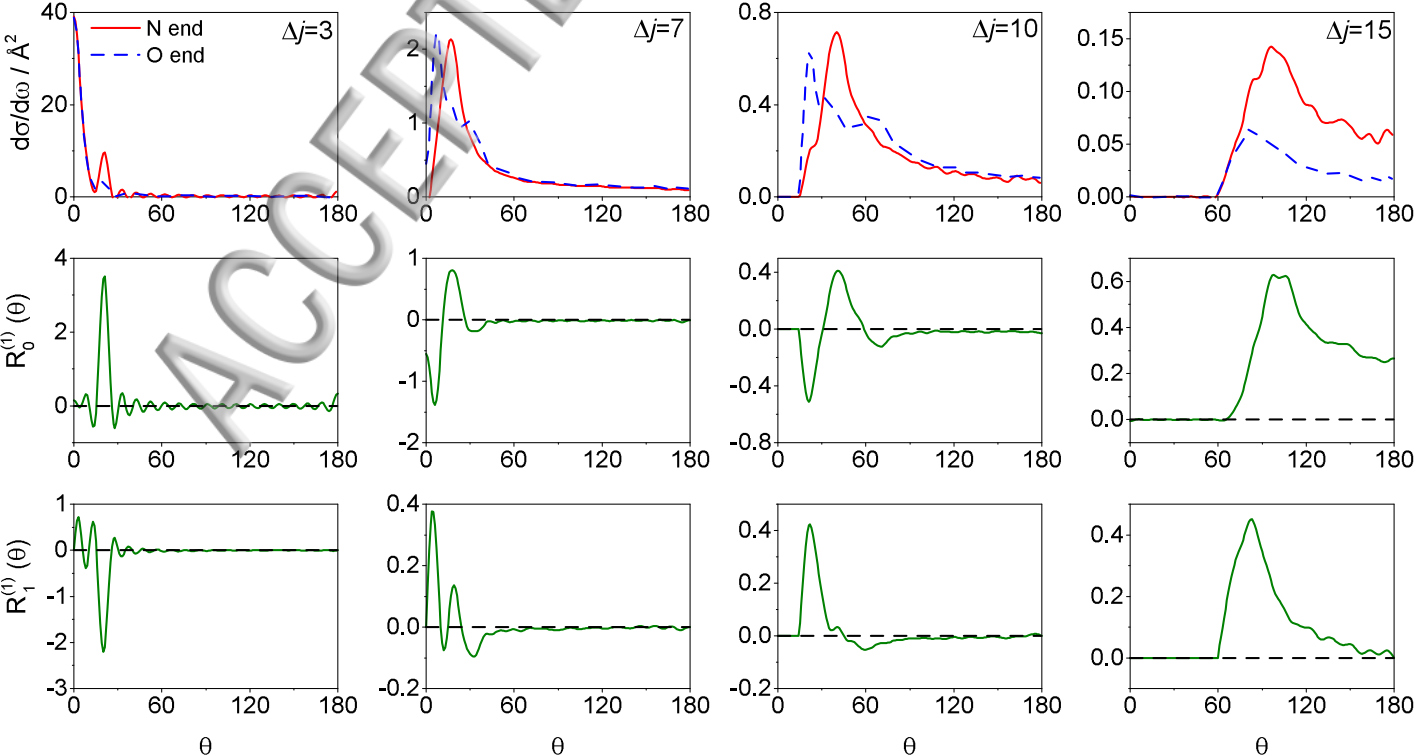

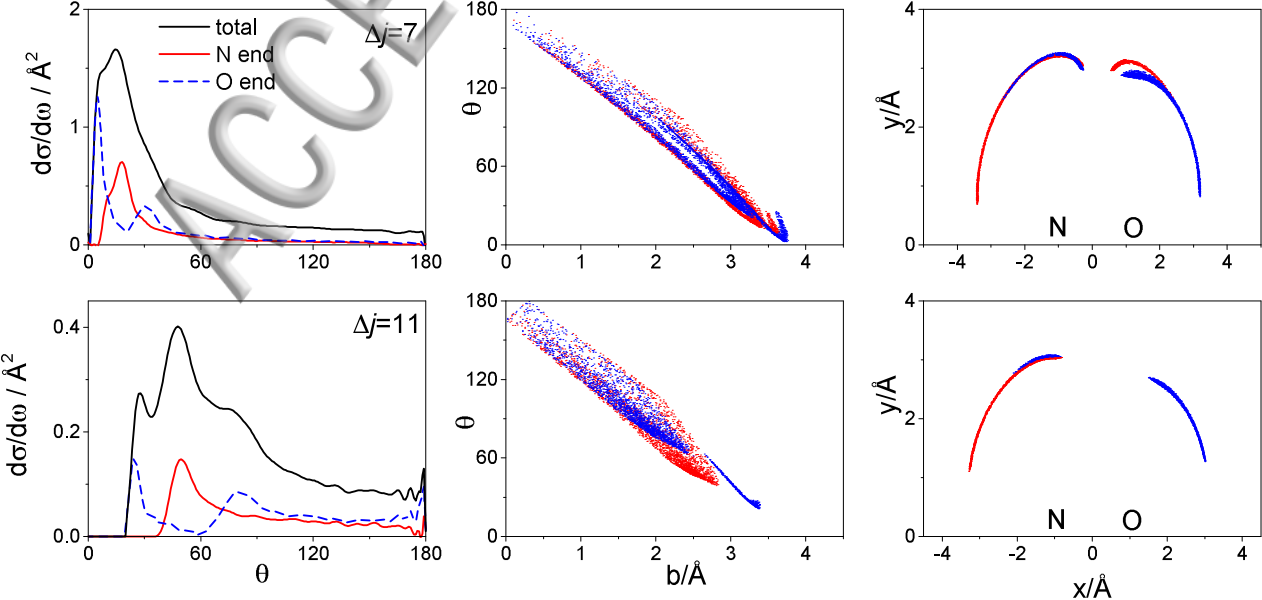
total
N end
O end
Δj=7
dσ/dω / Å²
θ
b/Å
y/Å
x/Å
N
O
Δj=11

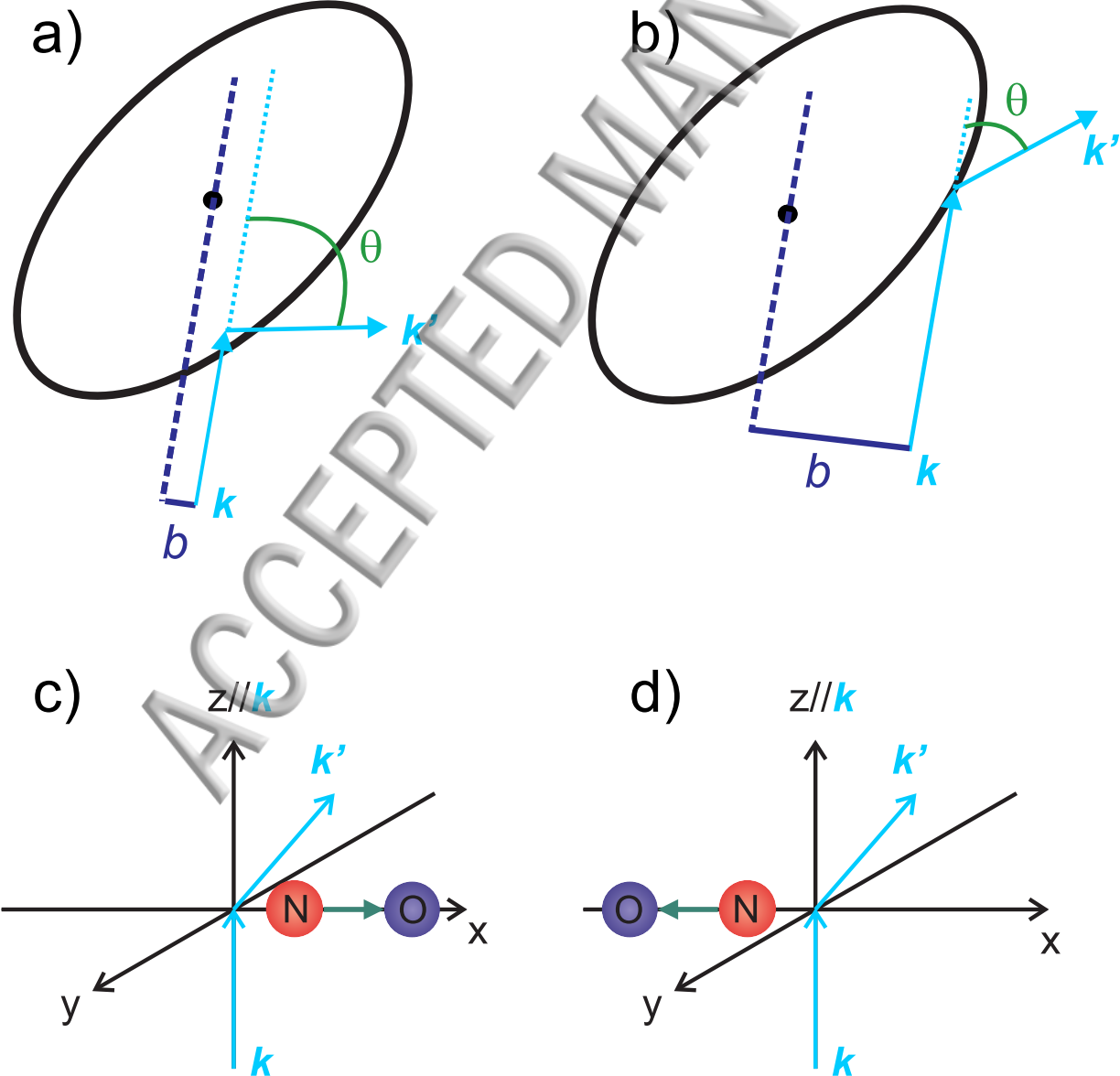

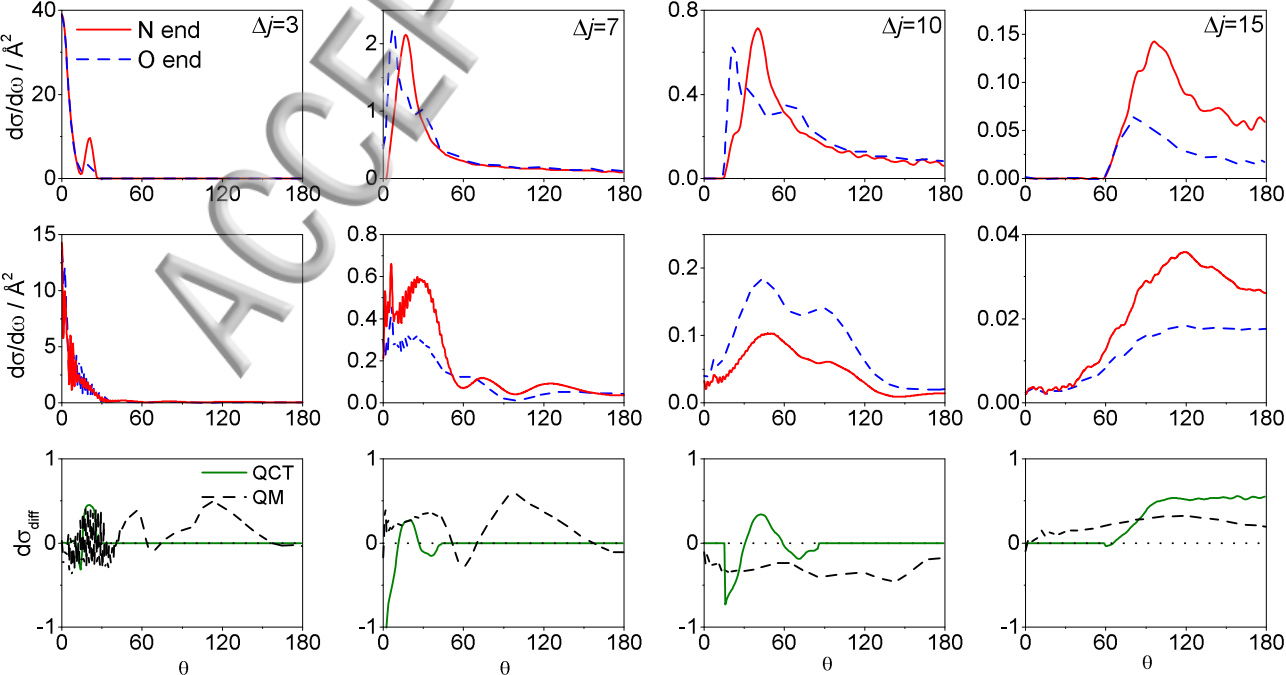
N end
O end
Δj=3
Δj=7
Δj=10
Δj=15
dσ/dω / Å²
dσ_diff
QCT
QM
θ

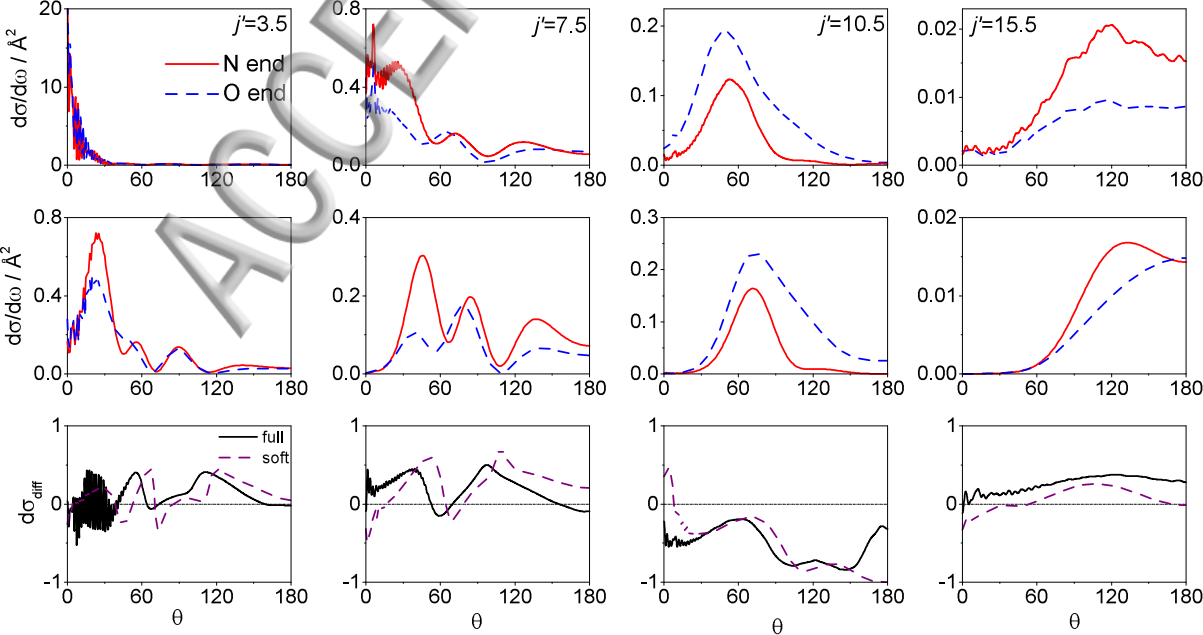
j'=3.5
j'=7.5
j'=10.5
j'=15.5
N end
O end
dσ/dω / Å²
dσ/dω / Å²
dσ_diff
full
soft
θ
θ
θ
θ